




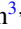


## Chemical control of polarization in thin strained films of a multiaxial ferroelectric: Phase diagrams and polarization rotation

Anna N. Morozovska <sup>1,\*</sup> Eugene A. Eliseev <sup>2</sup> Arpan Biswas <sup>3</sup> Hanna V. Shevliakova <sup>1</sup>  
Nicholas V. Morozovsky <sup>1</sup> and Sergei V. Kalinin <sup>3,†</sup>

<sup>1</sup>*Institute of Physics, National Academy of Sciences of Ukraine, pr. Nauky 46, 03028 Kyiv, Ukraine*

<sup>2</sup>*Institute for Problems of Materials Science, National Academy of Sciences of Ukraine, Krjijanovskogo 3, 03142 Kyiv, Ukraine*

<sup>3</sup>*Center for Nanophase Materials Sciences, Oak Ridge National Laboratory, Oak Ridge, Tennessee 37831, USA*



(Received 15 September 2021; revised 29 December 2021; accepted 7 March 2022; published 23 March 2022)

The emergent behaviors in thin films of a multiaxial ferroelectric (FE) due to electrochemical coupling between the rotating polarization and surface ions are explored within the framework of the 2–4 Landau-Ginzburg-Devonshire (LGD) thermodynamic potential combined with the Stephenson-Highland (SH) approach. The combined LGD-SH approach allows us to describe the electrochemical switching and rotation of a polarization vector in a multiaxial ferroelectric film covered by surface ions with a charge density defined by the oxygen pressure. We calculate phase diagrams, analyze the dependence of polarization components on the applied voltage, and discuss the peculiarities of quasistatic ferroelectric, dielectric, and piezoelectric hysteresis loops in thin strained multiaxial ferroelectric films. The nonlinear surface screening by oxygen ions makes the diagrams very different from the known diagrams of, e.g., strained BaTiO<sub>3</sub> films. Quite unexpectedly, we predict the appearance of ferroelectric reentrant phases. The obtained results point to the possibility to control the appearance and features of ferroelectric, dielectric, and piezoelectric hysteresis in multiaxial FE films covered with surface ions by varying their concentration via the partial oxygen pressure. The LGD-SH description of a multiaxial FE film can be further implemented within the Bayesian optimization framework, paving the way toward predictive materials optimization.

DOI: [10.1103/PhysRevB.105.094112](https://doi.org/10.1103/PhysRevB.105.094112)

### I. INTRODUCTION

Over the past 40+ years, ferroelectrics (FEs) have emerged as promising materials for electronic applications. The early proposals introduced the concept of a ferroelectric gate transistor [1,2]. The early 1990s saw advances in ferroelectric random-access memories [3–5] and, spurred by the advances in piezoresponse force microscopy [6–9], in ferroelectric data storage. The progress in ferroelectric film growth led to the concepts of ferroelectric tunneling barriers and multiferroic devices in the early 21st Century [10–12]. Notably, many of these applications have been demonstrated as prototypes and even as marketed devices. For classical oxide perovskites, the difficulties in materials integration invariably led to ferroelectric devices being overtaken by alternative technologies. However, the emergence of binary ferroelectrics such as hafnia and zirconia-based systems [13–15], magnesium-zinc oxides [16], and aluminum-scandium nitrides finally breaks this paradigm [17,18], and combined with the recent acute attention to microelectronic devices in the United States, it sets the stage for rapid progress in the field.

While the bulk properties of ferroelectrics are well understood and are generally amenable to characterization by

a broad variety of elastic and inelastic scattering techniques, this is not the case for ferroelectric surfaces and interfaces. In particular, the early field of ferroelectrics identified the crucial role of polarization screening on ferroelectric phase stability [19], namely that in the absence of screening or domain formation, depolarization fields will suppress the ferroelectric phase [20]. At that time, it was postulated that an accumulation of screening charges at the interfaces will compensate for the polarization charges, and detailed screening mechanisms were not considered. Later, the simplified approach in which potentials on surfaces are prescribed, along with the introduction of the concept of a ferroelectric dead layer, reflected the separation between screening and polarization bound charges. This dead layer model is now de-facto standard in the field of ferroelectrics [20–22], and it is used both for phenomenological modeling [23] and for the interpretation of the results of density functional modeling [24–26].

It should be noted that a rich body of work was developed in the concept of ferroelectrics-semiconductors. Here, the interplay between a ferroelectric and a semiconducting subsystem of the same material was considered, allowing us to account for the polarization-dependent photovoltaic [27–29] and photoelectrochemical [30,31] properties of ferroelectric surfaces. Interestingly, this direction is now seeing a resurgence with the rapid emergence of hybrid ferroelectric perovskites, in which ionic mobility is strongly coupled to photovoltaic [32,33] and domain formation phenomena [34,35].

\*Corresponding author: [anna.n.morozovska@gmail.com](mailto:anna.n.morozovska@gmail.com)

†[sergei2vk@gmail.com](mailto:sergei2vk@gmail.com); [sergei2@utk.edu](mailto:sergei2@utk.edu)

At the same time, very little theoretical work has been done in the context of ferroelectrics coupled to realistic surfaces and interfaces sustaining electrochemical and semi-conductive behaviors, i.e., having finite density of electronic or ionic states [36]. These scenarios correspond to realistic boundary conditions on open ferroelectric surfaces via ionic adsorption, which is intrinsically coupled to the surface electrochemical processes [37–39] and in integrated devices [23]. For open ferroelectric surfaces, there is now a preponderance of evidence on surface screening by adsorbed ions [40–42]. Previously, a theoretical formalism for an analysis of ferroelectric behavior in proximity to an electrochemically coupled interface was developed by Stephenson and Highland (SH) [43,44]. The Morozovska and Kalinin group [45–48] have developed this formalism further using the Landau-Ginzburg-Devonshire-Stephenson-Highland (LGD-SH) approach. They derived analytical solutions and relevant phase behaviors for *uniaxial* ferroelectrics in 2017, and recently for antiferroelectrics with electrochemical polarization switching [49,50]. The analysis [45–50] leads to the elucidation of *ferroionic* states, which are the result of nonlinear electrostatic interaction between ions with the surface charge density obeyed Langmuir adsorption isotherm and ferroelectric dipoles. The properties of these states were described by the system of coupled one-dimensional (1D) equations. However, the influence of surface ionic screening on the polar properties of *multiaxial* FE films covered by a layer of oxygen ions has not been considered theoretically, despite the fact that this case seems very interesting for fundamental research, is close to experiments, and is promising for applications.

To fill the gap in the knowledge, we extend the LGD-SH approach here to the very important case of *multiaxial* ferroelectrics, where the polarization can rotate depending on the surface electrochemical conditions and strain. Polarization rotation is broadly perceived as one of the fundamental mechanisms underpinning the enhanced electromechanical and dielectric properties of disordered ferroelectrics [51,52]. Similarly, the interplay between polarization rotation enabled by flat energy landscapes and disorder is broadly considered to be one of the mechanisms behind the unique functionalities of ferroelectric relaxors and morphotropic phase boundary materials [53,54].

Below we present the formalism for this analysis, construct phase diagrams as a function of pressure, temperature, and strain, and discover highly unusual behaviors, including the reentrant phase transitions between ferroelectric, ferroionic, and nonferroelectric states. We calculate and analyze the dependence of polarization, dielectric permittivity, and piezoelectric coefficients on applied voltage.

The manuscript is structured as following. Section II contains basic LGD equations and SH problem formulation with boundary conditions. Section III contains an analysis of the influence of mismatch strains and surface ions on the free energy of the film. Phase diagrams, ferroelectric, dielectric, and piezoelectric hysteresis loops are presented and analyzed in Sec. IV. Section V is a brief summary. Calculation details and auxiliary figures are listed in the Supplemental Material [55].

## II. LANDAU-GINZBURG-DEVONSHIRE-STEPHENSON-HIGHLAND APPROACH

### A. Problem formulation

Here we consider a system consisting of an electron-conducting substrate electrode, a multiaxial FE film of thickness  $h$ , covered with a layer of surface ions with a charge density  $\sigma$ . An in-plane mismatch strain  $u_m$  emerges due to the difference of the film and substrate lattice constants. As a rule, the modern epitaxial technique allows us to select the pair “perovskite film on perovskite substrate” with a given  $u_m$  in the range from  $-3\%$  (strongly compressed film) to  $3\%$  (strongly tensioned film) [56].

An ultrathin gap of width  $\lambda$  separates the film surface and the top electrode, which is either an ion-conductive planar electrode or an ion-blocking flatted apex of a scanning probe microscope (SPM) tip. In the latter case, the gap provides a direct ion exchange with an ambient medium, as shown in Fig. 1(a). The exchange is principally important for the considered problem because one needs to change freely the partial oxygen pressure, and the situation corresponded exactly with the experiments in Refs. [40–44]. Since oxygen atoms are very small, a gap wider than a lattice constant (e.g., 0.4–0.5 nm) can provide the exchange in the case of an ion-blocking electrode. In the case of perfect electric contact,  $\lambda = 0$ , the ion exchange is impossible for the ion-blocking electrode, but it is still possible for the ion-conducting one. Below, we consider  $\lambda$  as a parameter that varies continuously from 0 to several nm.

Due to the presence of an ultrathin dielectric gap between the top electrode and the surface of the film, the linear equation of state  $\mathbf{D} = \varepsilon_0 \varepsilon_d \mathbf{E}$  relates an electric displacement  $\mathbf{D}$  and field  $\mathbf{E}$  in the gap. Here  $\varepsilon_0$  is a universal dielectric constant, and  $\varepsilon_d \sim (1-10)$  is a relative permittivity in the gap filled by air with controllable oxygen pressure. A wide-band-gap FE film can be considered insulating, and its electric displacement is  $D_i = \varepsilon_0 \varepsilon_{ij}^b E_j + P_i$ , where  $i = 1, 2, 3$ , and  $\varepsilon_{33}^b$  is the relative background permittivity of the ferroelectric [22,57], and  $P_i$  denotes the ferroelectric polarization. The background is the contribution to the dielectric permittivity unrelated to the soft optic phonon mode responsible for the appearance of the ferroelectric polarization [22,57,58]. As a rule, it contains an electronic contribution and the contribution from other phonon modes, and so its value is rather small ( $4 \leq \varepsilon_{ij}^b \leq 10$ ) in comparison with ferroelectric permittivity [22,57]. However, neglecting the background effect and using the expression  $D_i = \varepsilon_0 E_i + P_i$  can significantly overestimate the depolarization field.

A potential  $\phi$  of a quasistatic electric field  $E_i$  satisfies a Laplace equation in the gap and a Poisson equation in the FE film. The electric boundary conditions, which are conventional, are as follows: the equivalence of the potential  $\phi$  to the applied voltage  $U$  at the top electrode (modeled by a flattened region  $x_3 = -\lambda$ ); the equivalence of the difference  $D_3^{(\text{gap})} - D_3^{(\text{film})}$  to the ionic surface charge density  $\sigma(\phi)$  at  $x_3 = 0$ ; the continuity of  $\phi$  at the gap-film interface  $x_3 = 0$ ; and zero potential at the conducting bottom electrode  $x_3 = h$  [see Fig. 1(a)].

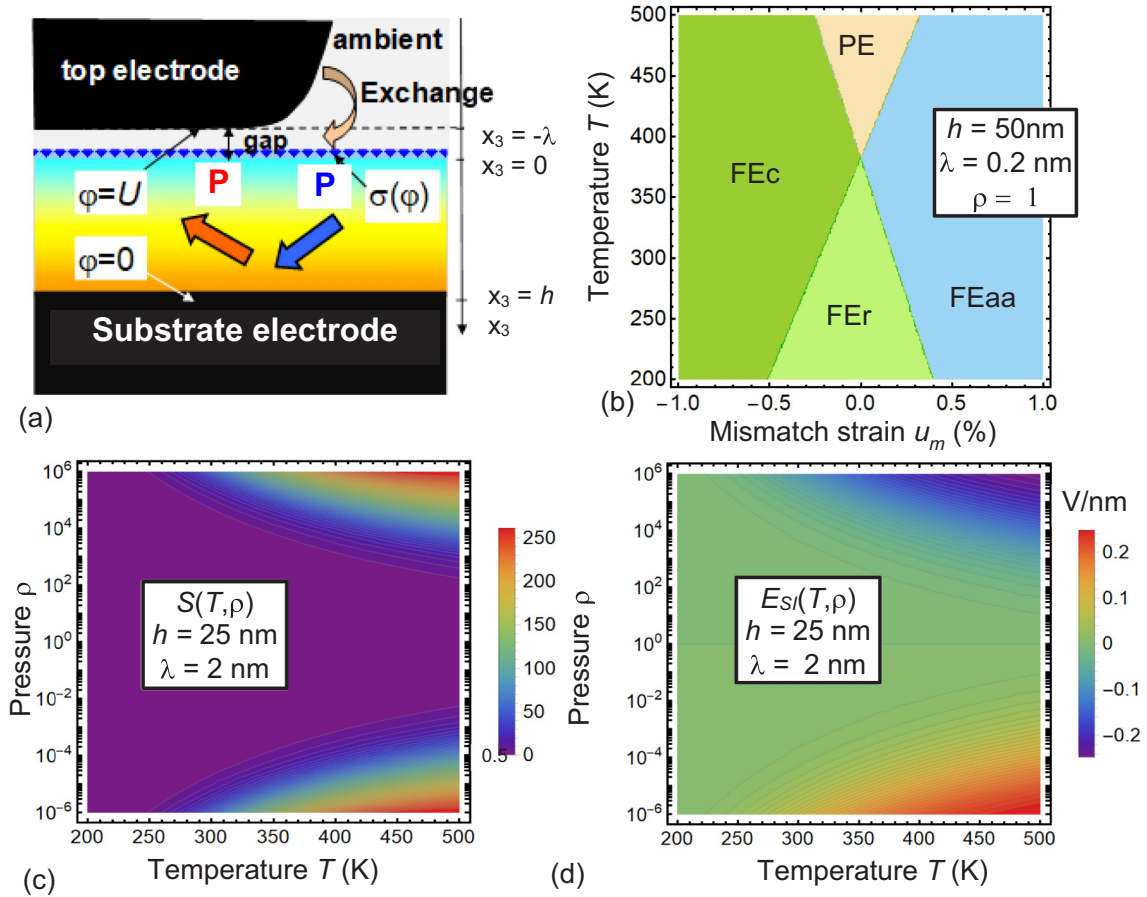


FIG. 1. (a) Layout of the considered system, consisting of an electron-conducting substrate electrode, a multiaxial FE film of thickness  $h$  with a polarization vector  $\mathbf{P}$ , a layer of surface ions with a charge density  $\sigma(\phi)$ , an ultrathin gap of width  $\lambda$  separating the film surface, and a top electrode providing a direct ion exchange with an ambient medium (from bottom to top). Adapted from Ref. [46]. (b) A typical phase diagram of a multiaxial FE film covered with perfect electrodes. Color maps of the surface charge entropy  $S(T, \rho, h)$  (c) and built-in field  $E_{Sl}(T, \rho, h)$  (d) in dependence on temperature  $T$  and relative oxygen pressure  $\rho$  calculated for  $h = 25\text{ nm}$  and  $\lambda = 2\text{ nm}$ . Other parameters and designations are listed in Tables I–III.

For the geometry used in this work, the ions are located exactly at the FE surface ( $x_3 = 0$ ), while in Ref. [43] they are located a distance  $\lambda$  away. Hence, a complete ionic compensation of the depolarizing field produced by the polarization bound charge is possible under favorable conditions (e.g., in some range of temperatures and pressures). It is important to note that the ions are in the electric potential  $\phi$ , which differs from the electrode potential  $U$  applied at a distance  $\lambda$  away from the FE surface. The effect of the gap thickness  $\lambda$  is thus different from Ref. [43], where Stephenson and Highland put  $\lambda = 0$  in the Langmuir adsorption isotherm.

To determine the spatial evolution of the long-range-order parameter-polarization components  $P_i$ , we use the combined SH-LGD approach, the mathematical details of which are described in Appendixes A and B of the Supplemental Material [55]. The LGD approach is based on the free-energy functional,  $F$ , which includes several contributions of different physical origins. The first is a bulk energy  $F_{\text{bulk}}$  of the film that is the Landau expansion on 2-4-6 powers of the polarization components  $P_i$ . Being negative in a ferroelectric state,  $F_{\text{bulk}}$  is responsible for the long-range polar order appearance. The

second contribution is the polarization gradient energy,  $F_{\text{grad}}$ , that is always positive in commensurate FE, and it increases in the vicinity of polarization inhomogeneities, e.g., near the surfaces, interfaces, and domain walls. The third is the electrostatic contribution of the film,  $F_{\text{el}}$ , the sign of which depends integrally on the polarization and electric field direction and magnitude. The fourth is the elastic and electrostriction contributions,  $F_{\text{els}}$ , the sign of which depends on the elastic strain and electrostriction coefficients. The fifth term is the film surface energy,  $F_S$ , that should be non-negative for the stability of the polar surface. The last term is the electrostatic energy of the gap,  $F_{\text{gap}}$ . Thus  $F$  has the form

$$F = F_{\text{bulk}} + F_{\text{grad}} + F_{\text{el}} + F_{\text{els}} + F_S + F_{\text{gap}}. \quad (1)$$

The mathematical forms of the contributions to Eq. (1) are

$$F_{\text{bulk}} = \int_{V_f} d^3r (a_i P_i^2 + a_{ij} P_i^2 P_j^2 + a_{ijk} P_i^2 P_j^2 P_k^2), \quad (2a)$$

$$F_{\text{grad}} = \int_{V_f} d^3r \frac{g_{ijkl}}{2} \left( \frac{\partial P_i}{\partial x_j} \frac{\partial P_k}{\partial x_l} \right), \quad (2b)$$

$$F_{\text{el}} = - \int_{V_f} d^3r \left( P_i E_i + \frac{\varepsilon_0 \varepsilon_b}{2} E_i E_i \right), \quad (2c)$$

$$F_{\text{cls}} = \int_{V_f} d^3r \left( Q_{ijkl} P_i P_j u_{kl} + \frac{s_{ijkl}}{2} u_{ij} u_{kl} \right), \quad (2d)$$

$$F_S = \frac{1}{2} \int_S d^2r a_{ij}^{(S)} P_i P_j. \quad (2e)$$

$$F_{\text{gap}} = - \int_{V_g} d^3r \frac{\varepsilon_0 \varepsilon_d}{2} E_i E_i - \int_S d^2r \frac{\phi}{2} \sigma_0. \quad (2f)$$

Here  $V_f$  is the film volume and  $V_g$  is the gap volume. The coefficients  $a_i$  depend linearly on the temperature  $T$ . In general, the tensor  $a_{ijk}$  and the polarization gradient tensor  $g_{ijkl}$  are positively defined and are also regarded as temperature-independent. Hereafter, we consider that  $a_{ij}$  is positively defined, and then one can disregard  $a_{ijk}$  for the ferroelectrics with the second-order phase transition. The electrostriction coefficients,  $Q_{ijkl}$ , can be of arbitrary sign. Elastic compliances are  $s_{ijkl}$ .

The influence of elastic strains  $u_{kl}$ , which are proportional to the mismatch strain  $u_m$ , via the electrostriction coupling term  $Q_{ijkl} P_i P_j u_{kl}$  can be approximately taken into account by the renormalization of the coefficients  $a_{ij}$  and  $a_{ijk}$  in Eq. (2a), e.g.,  $a_{ij} \rightarrow a_{ij} + Q_{ijkl} u_{kl}$  [59]. Thus, elastic strains via the electrostriction coupling can control the form of phase diagrams and preferable polarization direction in FE thin films [59]. The density of the film's electrostatic energy,  $P_i E_i + \frac{\varepsilon_0 \varepsilon_b}{2} E_i E_i$ , is dependent on the surface ionic charge  $\sigma_0$ , since the electric field is charge-dependent. Below we will study the joint action of mismatch strains and surface ionic charge on the polar state of the ferroelectric film. Note that the density of the gap energy [Eq. 2(f)] can be identically rewritten as the product of the ionic charge  $\sigma_0(\phi)$  and electric potential  $\phi$ , at which point the factor  $1/2$  disappears [60].

An equation for the surface ionic charge density  $\sigma_0(\phi)$  is analogous to the Langmuir adsorption isotherm [61] used in interfacial electrochemistry for the electrochemical species adsorption onto a solid surface. The dependence of the equilibrium charge density  $\sigma_0(\phi)$  on the electric potential  $\phi$  is controlled by the concentration of surface ions,  $\theta_i(\phi)$ , at the interface  $x_3 = 0$  in a self-consistent manner, as proposed by Highland *et al.* [43] and Stephenson *et al.* [44]:

$$\begin{aligned} \sigma_0(\phi) &= \sum_{i=1}^2 \frac{e Z_i \theta_i(\phi)}{A_i} \\ &\equiv \sum_{i=1}^2 \frac{e Z_i}{A_i} \left[ 1 + \rho^{-1/n_i} \exp \left( \frac{\Delta G_i^{00} + e Z_i \phi}{k_B T} \right) \right]^{-1}. \quad (3) \end{aligned}$$

Here  $e$  is an elementary charge,  $Z_i$  is the ionization degree of the surface ions/electrons, and  $1/A_i$  are saturation densities of the surface ions. The subscript  $i$  designates the summation on positive ( $i = 1$ ) and negative ( $i = 2$ ) charges, respectively;  $\rho = \frac{p_{\text{O}_2}}{p_{\text{O}_2}^0}$  is the relative partial pressure of oxygen (or other ambient gas) [44], and  $n_i$  is the number of surface ions created per gas molecule. Two surface charge species exist, since the gas molecule had been electroneutral before its electrochemical

decomposition started. The dimensionless ratio  $\rho$  varies in a relatively wide range from  $10^{-6}$  to  $10^6$  [43,44].

Positive parameters  $\Delta G_1^{00}$  and  $\Delta G_2^{00}$  are the free energies of the surface defect formation at normal conditions,  $p_{\text{O}_2}^0 = 1$  bar, and zero applied voltage  $U = 0$ . The energies  $\Delta G_i^{00}$  are responsible for the formation of different surface charge states (ions, vacancies, or their complexes). Specifically, exact values of  $\Delta G_i^{00}$  are poorly known even for many practically important cases, and so hereafter they are regarded as varying in the range  $\sim(0-1)$  eV [43,44]. Notably, the developed solutions are insensitive to the specific details of the charge compensation process [62], but they are sensitive to the thermodynamic parameters of corresponding reactions [63].

The expression for  $\sigma_0(\phi)$  is taken from Refs. [43,44], where it was applied for ferroelectric surfaces, and corresponding explanations based on electrochemistry are given in the references cited therein. It should be noted that, when oxygen ions meet free electrons at the tip electrode, there may be some kind of electrochemical reaction leading either to electrode oxidation or oxygen molecule formation. Possible changes of the tip electrode state are not considered either by Stephenson and Highland or by us. We assume that the voltage applied between the tip and the bottom electrode is independent of the electrochemical processes, which may take place at the tip surface.

It is also important to note that while Eq. (3) pertains to a specific case of surface electrochemical reaction, the proposed formalism is considerably more universal. Equations (1)–(3) jointly define the coupling between the polarization  $P_i$ , the electric potential  $\phi$ , and the potential-dependent surface screening charge  $\sigma_0[\phi]$ . As such, this formalism can be readily adapted to other electrochemical models, or to the specific functional form of interface density of electronic or ionic states.

## B. Single-domain approximation

Since the stabilization of single-domain polarization in ultrathin perovskite films takes place due to the chemical switching, we can assume the absence of domain structure in the ferroelectric film (see, e.g., Refs. [40–44]). In a general case, the polarization can change significantly in the  $x_3$ -direction, especially near the film surfaces. To minimize the effect, we also assume that the surface energy is negligibly small ( $a_{ij}^{(S)} \rightarrow 0$ ), which corresponds to the so-called natural boundary conditions,  $\frac{\partial P_i}{\partial n} |_S = 0$ . Assuming that  $a_{ij}^{(S)} = 0$ , we can neglect the gradient terms in a single-domain approximation and note that the distribution  $P_i(\vec{x})$  does not deviate significantly from the values  $\langle P_i \rangle$  averaged over the film thickness, namely  $P_i \cong \langle P_i \rangle$ .

Neglecting the sixth-order terms of polarization, polarization gradient energy, and surface energy, the free energy density (2) per unit area acquires the form

$$\begin{aligned} f &= \left( a_i P_i^2 + a_{ij} P_i^2 P_j^2 + Q_{ijkl} P_i P_j u_{kl} + \frac{s_{ijkl}}{2} u_{ij} u_{kl} - E_3 P_3 \right. \\ &\quad \left. - \varepsilon_0 \varepsilon_{33} \frac{E_3^2}{2} \right) h - \frac{\varepsilon_0 \varepsilon_d}{2} \frac{(\Psi - U)^2}{\lambda} + \int_0^\Psi \sigma_0(\varphi) d\varphi. \quad (4) \end{aligned}$$

Here we assume that the in-plane components of the external electric field,  $E_{1,2}$ , are absent, and the out-of-plane component of the field,  $E_3$ , is proportional to the “effective” electric potential  $\Psi$  [49]:

$$E_3 = \frac{\Psi}{h}. \quad (5)$$

The expression for the effective potential  $\Psi$  has the form [49]

$$\Psi = h \frac{\lambda(\sigma_0(\Psi) - P_3) + \varepsilon_0 \varepsilon_d U}{\varepsilon_0(\varepsilon_d h + \lambda \varepsilon_{33}^b)}. \quad (6)$$

Note that Eqs. (5) and (6) for  $E_3$  and  $\Psi$  arise from the boundary conditions for  $D_3$  discussed in Sec. II A. The surface charge density  $\sigma_0(\Psi)$  is given by Eq. (3).

It is seen from Eqs. (5) and (6) that the out-of-plane electric field,  $E_3 = \frac{\lambda(\sigma_0(\Psi) - P_3) + \varepsilon_0 \varepsilon_d U}{\varepsilon_0(\varepsilon_d h + \lambda \varepsilon_{33}^b)}$ , consists of the external field, the depolarization field, and the field created by the surface ion layer. The effective potential  $\Psi$  contains the contribution from surface charges  $\sigma_0$ , the depolarization field contribution proportional to  $P_3$ , and the external potential drop proportional to applied voltage  $U$ . The electrostatic potential  $\phi$  is equal to the effective potential  $\Psi$  at the location of surface charges,  $x_3 = 0$ . Note that the SH model [43] neglects the effects of background permittivity, while the expression (6) contains the effect due to the presence of the gap (see the denominator  $\varepsilon_d h + \lambda \varepsilon_{33}^b$ ). The sign of the ionic charge  $\sigma_0$  that compensates the polarization is opposite to that in Ref. [44], because here a positive  $P_3$  points away from the interface. Thus, all expressions involving the term  $(\sigma_0(\Psi) - P_3)$  are equivalent to the terms  $(\sigma_0 + P_3)$  in Ref. [44].

### III. FREE ENERGY OF THE FERROIONIC SYSTEM: POSSIBLE PHASES

#### A. The influence of mismatch strains and surface ion charge on free-energy coefficients

Following Pertsev *et al.* [59], the coefficients  $a_i$  in Eq. (5a) must be renormalized by a mismatch strain  $u_m$ , which can change their sign for high enough compressive or tensile  $|u_m|$ . The coefficients  $a_{ij}$  in the same equation can change sign from negative to positive due to the electrostriction coupling with a substrate. Below we consider the FE films with a cubic  $m3m$  symmetry of the parent phase that allows us to use analytical results [59] for the renormalization of the coefficients  $a_i$  and  $a_{ij}$  by the mismatch strain and electrostriction.

Assuming that  $|eZ_i\Psi/k_B T| \ll 1$ , the potential density (4) can be further expanded in  $P_i$  and  $\Psi$  powers [48–50]. As a result, we obtain the expression for the “effective” free-energy density from Eq. (4):

$$f = b_1(P_1^2 + P_2^2) + b_3P_3^2 + b_{11}(P_1^4 + P_2^4) + b_{33}P_3^4 + b_{12}P_1^2P_2^2 + b_{13}(P_1^2 + P_2^2)P_3^2 - P_3\tilde{E}_3, \quad (7)$$

whose coefficients, derived in Appendix B of the Supplemental Material [55], depend on the mismatch strain  $u_m$ , oxygen pressure  $\rho$ , and temperature  $T$  in the following

way:

$$b_3(T, \rho, h, u_m) = \left( a_1(T) - \frac{2Q_{12}u_m}{s_{11} + s_{12}} \right) (1 + S(T, \rho, h)) + \frac{\lambda}{2\varepsilon_0(\varepsilon_d h + \lambda \varepsilon_{33}^b)}, \quad (8a)$$

$$b_1(T, u_m) = a_1(T) - u_m \frac{Q_{11} + Q_{12}}{s_{11} + s_{12}}, \quad (8b)$$

$$b_{11} = a_{11} + \frac{s_{11}(Q_{11}^2 + Q_{12}^2) - 2Q_{11}Q_{12}s_{12}}{2(s_{11}^2 - s_{12}^2)}, \quad (8c)$$

$$b_{33}(T, \rho, h) = \left( a_{11} + \frac{Q_{12}^2}{s_{11} + s_{12}} \right) (1 + S(T, \rho, h)), \quad (8d)$$

$$b_{12} = a_{12} - \frac{s_{12}(Q_{11}^2 + Q_{12}^2) - 2Q_{11}Q_{12}s_{11}}{s_{11}^2 - s_{12}^2} + \frac{Q_{44}^2}{2s_{44}}, \quad (8e)$$

$$b_{13}(T, \rho, h) = \left( a_{12} + \frac{Q_{12}(Q_{11} + Q_{12})}{s_{11} + s_{12}} \right) (1 + S(T, \rho, h)). \quad (8f)$$

The coefficient  $a_1(T) = \alpha_T(T - T_C)$  changes sign at Curie temperature  $T_C$ , and the inverse Curie constant  $\alpha_T > 0$ . Coefficients  $Q_{ij}$  are electrostriction tensor components, and  $s_{ij}$  are elastic compliances in Voight notation. The inequalities  $b_{11} > 0$ ,  $b_{33} > 0$ ,  $b_{12} > -2b_{11}$ , and  $b_{13} > -2\sqrt{b_{11}b_{33}}$  should be valid for the LGD potential stability. The first term in the coefficient  $b_3(T, \rho, h, u_m)$ , and the coefficients  $b_{33}(T, \rho, h)$  and  $b_{13}(T, \rho, h)$ , are proportional to the factor  $(1 + S(T, \rho, h))$ , where the positive function  $S(T, \rho, h)$  is induced by the surface charge as

$$S(T, \rho, h) = \frac{\lambda h}{\varepsilon_0(\varepsilon_d h + \lambda \varepsilon_{33}^b)} \sum_{i=1,2} \frac{(eZ_i f_i(T, \rho))^2}{A_i k_B T}, \quad (9a)$$

where

$$f_i(T, \rho) = \left[ 1 + \rho^{-1/n_i} \exp\left(\frac{\Delta G_i^{00}}{k_B T}\right) \right]^{-1}. \quad (9b)$$

The function  $S(T, \rho, h)$  may be interpreted as the constituted parts of the positive and negative surface charge configuration entropy, which depend on temperature, oxygen partial pressure, film thickness, and gap width. The functions  $f_i(T, \rho)$  can be interpreted as filling factors in the statistical sum. Comparing their expressions with, e.g., the Fermi-Dirac distribution function  $f(T, E) = (1 + g \exp(\frac{E}{k_B T}))^{-1}$ , where  $g$  is a degeneracy factor, we can associate  $g \sim \rho^{-1/n_i}$  and  $E \sim \Delta G_i^{00}$ . Below we use the terms “surface charge entropy” and “filling factors” to refer to the functions  $S(T, \rho, h)$  and  $f_i(T, \rho)$ , respectively.

The second term in Eq. (8a) proportional to the gap width,  $\frac{\lambda}{2\varepsilon_0(\varepsilon_d h + \lambda \varepsilon_{33}^b)}$ , originates from the depolarization field. The effective electric field  $\tilde{E}_3$  in Eq. (7) is a sum of a built-in field

TABLE I. Homogeneous ferroelectric phases, the spontaneous order parameters, and free energy of the phases at zero total field,  $E_{\text{SI}}(T, \rho, h) + E_a(U, h) = 0$ .

Phase	Spontaneous order parameters	Free energy $f_R$
PE	$P_1 = P_2 = P_3 = 0$	0
FEa	$P_1 = \pm \sqrt{-\frac{b_1}{2b_{11}}}, P_2 = P_3 = 0$	$-\frac{b_1^2}{4b_{11}}$
FEc	$P_3 = \pm \sqrt{-\frac{b_3}{2b_{33}}}, P_1 = P_2 = 0$	$-\frac{b_3^2}{4b_{33}}$
FEaa	$P_1 = \mp P_2 = \pm \sqrt{-\frac{b_1}{2b_{11}+b_{12}}}, P_3 = 0$	$-\frac{b_1^2}{(2b_{11}+b_{12})}$
FEac	$P_1 = \pm \sqrt{-\frac{2b_{33}b_1 - b_{13}b_3}{4b_{11}b_{33} - b_{13}^2}}, P_3 = \pm \sqrt{-\frac{2b_{11}b_3 - b_{13}b_1}{4b_{11}b_{33} - b_{13}^2}}, P_2 = 0$	$\frac{-b_{33}b_1^2 - b_{11}b_3^2 + b_{13}b_1b_3}{(4b_{11}b_{33} - b_{13}^2)}$
FEr	$P_1 = \mp P_2 = \frac{\pm \sqrt{b_3b_{13} - 2b_1b_{33}}}{\sqrt{2(2b_{11}+b_{12})b_{33} - 2b_{13}^2}}, P_3 = \pm \frac{\sqrt{-b_3(2b_{11}+b_{12}) + 2b_1b_{13}}}{\sqrt{2(2b_{11}+b_{12})b_{33} - 2b_{13}^2}}$	$\frac{-b_3^2(2b_{11}+b_{12}) - 4b_1^2b_{33} + 4b_1b_3b_{13}}{4(2b_{11}+b_{12})b_{33} - b_{13}^2}$

$E_{\text{SI}}$  and an acting field  $E_a$ :

$$\tilde{E}_3(T, \rho, h) = E_{\text{SI}}(T, \rho, h) + E_a(U, h), \quad (10a)$$

$$E_{\text{SI}}(T, \rho, h) = \frac{\lambda}{\varepsilon_0(\varepsilon_d h + \lambda \varepsilon_{33}^b)} \sum_{i=1,2} \frac{eZ_i}{A_i} f_i(T, \rho), \quad (10b)$$

$$E_a(U, h) = -\frac{\varepsilon_d U}{\varepsilon_d h + \lambda \varepsilon_{33}^b}. \quad (10c)$$

The built-in field  $E_{\text{SI}}(T, \rho, h)$  created by surface ions is significant for thin film, being proportional to the ratio  $\frac{\lambda}{h}$ . Since, as a rule,  $\varepsilon_d h \gg \lambda \varepsilon_{33}^b$ , the acting field is close to an external field,  $E_a \approx E_e = -\frac{U}{h}$ . Also, we need to support positive  $b_{11}$ ,  $b_{12}$ , and  $b_{33}$  in the actual temperature range by the electrostriction coupling, and to select an appropriate mismatch strain to support either in-plane or out-of-plane polarization that couples with a surface electrochemistry.

It is seen from Eqs. (8)–(10) that the influence of the relative partial oxygen pressure on the multiaxial FE film reduces to the influence of the surface charge  $\sigma_0[\phi]$  caused by the adsorption/desorption of oxygen ions, mathematically expressed via the surface charge entropy  $S(T, \rho, h)$  and the built-in electric field  $E_{\text{SI}}(T, \rho, h)$  penetrating the entire depth of the film.

The static behavior of the polarization components,  $P_i$ , is described via the nonlinear algebraic equations, which follow from the minimization of the free energy (7),  $\frac{\partial f}{\partial P_i} = 0$ :

$$(2b_1 + 4b_{11}P_1^2 + 2b_{12}P_2^2 + 2b_{13}P_3^2)P_1 = 0, \quad (11a)$$

$$(2b_1 + 4b_{11}P_2^2 + 2b_{12}P_1^2 + 2b_{13}P_3^2)P_2 = 0, \quad (11b)$$

$$(2b_3 + 4b_{33}P_3^2 + 2b_{13}(P_1^2 + P_2^2))P_3 = E_{\text{SI}}(T, \rho, h) + E_a(U, h). \quad (11c)$$

## B. The table of homogeneous phases and material parameters

Homogeneous FE phases, the spontaneous order parameters, and free energy (4) of the phases at  $E_i = 0$  are listed in Table I. The abbreviations ‘‘PE’’ and ‘‘FE’’ denote the paraelectric and ferroelectric phases, respectively. The classification and designations of FE phases are very well known [59] and come from the classification of domains with a different orientation of polarization. They are based on the letter-type ‘‘code’’ for zero and nonzero components of  $\mathbf{P}$  under the absence of a total electric field. The nonzero components 1, 2, and 3 are denoted with letters ‘‘a,’’ ‘‘b,’’ or ‘‘c,’’ respectively. If the same letter ‘‘a’’ is used twice, it means that  $P_1 = \pm P_2$ . For the sake of brevity, we use the letter ‘‘r’’ for the ‘‘abc’’ or ‘‘aac’’ cases, since it is a rhombohedral phase.

We also note that the built-in electric field  $E_{\text{SI}}$  cannot induce new FE phases with reversible polarization, but it can induce the electret-like ferrielectric (FEI) phase (not listed in Table I) instead of the PE phase (listed in Table I). The FEI phase is characterized by a spontaneous polarization that is absent in the PE phase. The boundary between the FEI and PE phases is diffuse, and only that part of the PE phase corresponding to  $\rho \ll 1$  (or  $\rho \gg 1$ ) becomes the FEI phase. Of course, the built-in field can induce the polarization component  $P_3$  in the FEaa phase, but it is electret-like and not bistable. Simple analytical expressions for the FEI phase energy and electret-like polarization components are absent.

Table II contains the material parameters of a hypothetical bulk ferroelectric close to BaTiO<sub>3</sub>, used in this work. From the table, the coefficient  $a_{11} = 3.6(T + 222) \times 10^6 \text{ m}^5 \text{ J/C}^4$  is positive at all temperatures. In contrast, the value  $a_{11} = 3.6(T - 448) \times 10^6 \text{ m}^5 \text{ J/C}^4$ , used by Pertsev *et al.* [59], is negative below 448 K. The electrostriction coupling term,

TABLE II. LGD coefficients and other material parameters of a bulk BaTiO<sub>3</sub>.

Coefficient	Numerical value	Refs.
$\varepsilon_{33}^b$ (dimensionless)	7	[64]
$a_i$ (mJ/C <sup>2</sup> )	$a_1 = \alpha_T(T - T_C)$ , $\alpha_T = 3.3 \times 10^5$ , $T_C = 383$	[59]
$a_{ij}$ (m <sup>5</sup> J/C <sup>4</sup> )	$a_{11} = 3.6(T + 222) \times 10^6$ (this work), $a_{12} = 4.9 \times 10^8$ (Ref. [59])	This work
$Q_{ij}$ (m <sup>4</sup> /C <sup>2</sup> )	$Q_{11} = 0.11$ , $Q_{12} = -0.043$ , $Q_{44} = 0.059$	[65]
$s_{ij}$ (Pa <sup>-1</sup> )	$s_{11} = 8.3 \times 10^{-12}$ , $s_{12} = -2.7 \times 10^{-12}$ , $s_{44} = 9.24 \times 10^{-12}$	[66]
$h$ (nm)	5–50	Variable

TABLE III. Geometrical, surface ion-related, and interfacial parameters.

Description	Designation and dimensionality	Substrate/BaTiO <sub>3</sub> film/ionic charge/gap/tip
Film thickness	$h$ (nm)	Vary from 5 to 50 nm
Mismatch strain	$u_m$ (dimensionless)	Variable
Equilibrium surface charge density	$\sigma_0(\phi)$ (C/m <sup>2</sup> )	Variable
Occupation degree of surface ions	$\theta i$ (dimensionless)	Variable
Relative oxygen partial pressure	$\rho$ (dimensionless)	Vary from 10 <sup>-6</sup> to 10 <sup>6</sup>
Width of the dielectric gap	$\lambda$ (nm)	0.2–2
Permittivity of the dielectric gap	$\epsilon_d$ (dimensionless)	1–10
Universal dielectric constant	$\epsilon_0$ (F/m)	$8.85 \times 10^{-12}$
Electron charge	$e$ (C)	$1.6 \times 10^{-19}$
Ionization degree of the surface ions	$Z_i$ (dimensionless)	$Z_1 = +2, Z_2 = -2$
Number of surface ions created per oxygen molecule <sup>a</sup>	$n_i$ (dimensionless)	$n_1 = -2, n_2 = +2$
Saturation area of the surface ions	$A_i$ (m <sup>2</sup> )	$A_1 = A_2 = A = 10^{-18}$
Surface defect/ion formation energy	$\Delta G_i^{00}$ (eV)	0.1–0.3, we suggest $\Delta G_1^{00} = \Delta G_2^{00} = \Delta G = 0.2$

<sup>a</sup>There was a repeated typographical error in earlier works [44–47], where we regard that  $n_1 = +2, n_2 = -2$ . This difference leads to the different signs of the built-in field [see Eqs. (9) and (10b) in this work], while other results, such as phase diagrams, remained the same under the conditions  $n_1 = -n_2, Z_1 = -Z_2, A_1 = A_2 = A$ , and  $\Delta G_1^{00} = \Delta G_2^{00} = \Delta G$ .

$\frac{s_{11}(Q_{11}^2 + Q_{12}^2) - 2Q_{11}Q_{12}s_{12}}{2(s_{11}^2 - s_{12}^2)}$ , appeared too small to make the Pertsev *et al.* coefficient  $b_{11}$  positive above 245 K, requiring inclusion of the higher terms in Eq. (4), which are proportional to  $a_{ijk}$ . Since the inclusion of the higher terms prevents us from deriving analytical results, we use positive  $a_{11}$  from Table II and neglect the higher terms. The results listed in Table I are used in this work, and, as will be demonstrated in the next section, the selected positive value of  $a_{11}$  leads to the phase diagram structure similar to the one calculated by Pertsev *et al.* for BaTiO<sub>3</sub> [compare Figs. 1(b) and 1(a) from Ref. [59]].

Table III contains surface ion-related, geometrical, and interfacial parameters. As follows from the table, the surface charge entropy

$$S(T, \rho, h) = S\left(T, \frac{1}{\rho}, h\right) \sim \frac{(2e)^2}{Ak_B T} \left( \frac{1}{1 + \rho^2 \exp\left(\frac{\Delta G}{k_B T}\right)} + \frac{1}{1 + \rho^{-2} \exp\left(\frac{\Delta G}{k_B T}\right)} \right)^{-2} \quad (12a)$$

in accordance with Eq. (9), because  $n_1 = -n_2 = -2, Z_1 = -Z_2 = 2, A_1 = A_2 = A$ , and  $\Delta G_1^{00} = \Delta G_2^{00} = \Delta G$ . Thus, the physical state calculated for  $\rho \neq 1$  coincides with the state calculated for  $1/\rho$ . Therefore, hereafter we analyze the case  $0 \leq \rho \leq 1$  only. The condition  $0 \leq \rho \leq 1$  is more easily realizable experimentally in comparison with the condition  $0 \leq \rho < \infty$ . We also note that the built-in field

$$E_{Si}(T, \rho, h) = -E_{Si}\left(T, \frac{1}{\rho}, h\right) \sim \frac{2e}{A} \left( \frac{1}{1 + \rho^2 \exp\left(\frac{\Delta G}{k_B T}\right)} - \frac{1}{1 + \rho^{-2} \exp\left(\frac{\Delta G}{k_B T}\right)} \right) \quad (12b)$$

in accordance with Eq. (10b), so it vanishes at  $\rho \rightarrow 1$  and changes its sign under the condition  $\rho \rightarrow \frac{1}{\rho}$  [see Fig. 1(d) for details].

In accordance with Table III,  $\frac{\Delta G_i^{00}}{k_B T} > 4$  for  $\Delta G_i^{00} \geq 0.1$  eV and  $|T| < 500$  K, making the factor  $\exp\left(\frac{\Delta G_i^{00}}{k_B T}\right) \gg 1$  in the actual temperature range. Therefore, the surface charge entropy  $S(T, \rho, h)$  can strongly change with pressure. Actually,  $S(T, \rho, h)$  is minimal for  $\rho = 1$ , namely  $S(T, 1, h) \ll 1$  at  $T = 200$  K. At the same time,  $S(T, \rho, h)$  increases monotonically with  $\rho$  deviation from unity reaching several hundred at  $\rho = 10^{-6}$  and  $T = 500$  K [see Fig. 1(c) for details]. Hence the multiplier  $(1 + S(T, \rho, h))$  can significantly increase the absolute value of the negative coefficient  $(a_1(T) - \frac{2Q_{12}u_m}{s_{11} + s_{12}})$ . As a result, the coefficient  $b_3(T, \rho, h, u_m)$  can become more negative than  $b_1(T, u_m)$ . The circumstance opens the possibility of the out-of-plane polarization emergence at high ( $\rho \gg 1$ ) or low ( $\rho \ll 1$ ) partial oxygen pressures in ultrathin multiaxial FE films. Below we will demonstrate the possibility and analyze the conditions of its appearance.

## IV. RESULTS

### A. Phase diagrams in coordinate temperature-mismatch strain

The temperature-mismatch phase diagram calculated for a thick multiaxial FE film covered with perfect electrodes is shown in Fig. 1(b). The film is short-circuited, i.e.,  $E_a = 0$ . Since the gap and oxygen pressure effect are absent for the film, the diagram is very similar to the diagram of a strained BaTiO<sub>3</sub> film calculated by Pertsev *et al.* [59]. The values of the used constants are listed in Table II. The phase diagrams are calculated using the formulas in Table I and visualized in MATHEMATICA 12.2 [67].

There is a PE phase and three FE phases in Fig. 1(b), namely the FEc phase with nonzero out-of-plane polarization  $P_3$ , the FEaa phase with nonzero in-plane polarization components,  $P_1 = P_2$ , and the mixed FER phase with nonzero  $P_3$  and  $P_1 = P_2$ . The FEc phase is stable at compressive mismatch strains  $u_m < 0$  (mainly  $u_m < -0.5\%$ ), the PE phase is stable at temperatures higher than 400 K and small  $|u_m| < 0.5\%$ ,

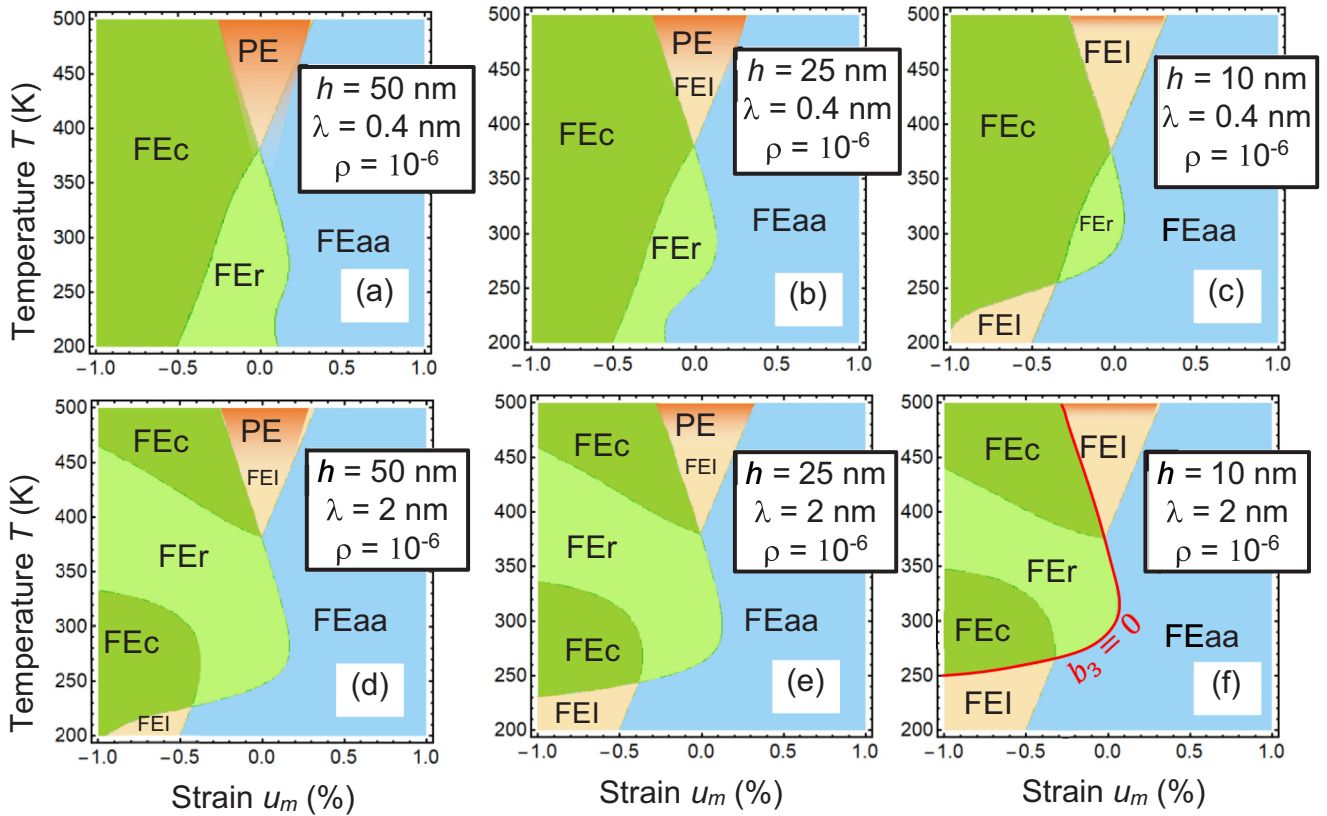


FIG. 2. Typical phase diagrams of a multiaxial FE film in dependence on the temperature  $T$  and mismatch strain  $u_m$ . A red curve in the plot (f) corresponds to the condition  $b_3 = 0$ . The values of relative partial oxygen pressure  $\rho$ , gap thickness  $\lambda$ , and film thickness  $h$  are listed for each plot. Other parameters are listed in Tables II and III;  $U = 0$ .

the FEaa phase is stable at tensile strains  $u_m > 0$  (mainly  $u_m > -0.5\%$ ), and the FEr phase is stable at  $T < 400$  K and  $|u_m| < 0.5\%$ . The boundaries between these four phases are straight lines, which cross in a single point, where all the phases have the same value of free energy. In accordance with Table I, the PE-FEaa boundary is given by the equation  $b_1(T, u_m) = 0$ , the PE-FEc boundary is given by the equation  $b_3(T, u_m) = 0$ , and the FEc-FEr and FEr-FEaa boundaries are given by the equality of the corresponding energies.

For the prototype BaTiO<sub>3</sub> parameters listed in Table II, compressive strains support the out-of-plane polarization component  $P_3$ , since  $Q_{12} < 0$  and the negative term  $-\frac{2Q_{12}u_m}{s_{11}+s_{12}}$  decreases the coefficient  $b_3$  in Eq. (8a). Tensile strains support the in-plane polarization components  $P_{1,2}$ , since  $Q_{11} + Q_{12} > 0$ , and the negative term  $-u_m \frac{Q_{11}+Q_{12}}{s_{11}+s_{12}}$  decreases the coefficient  $b_1$  in Eq. (8b).

The diagrams in Fig. 2 illustrate how the presence of oxygen pressure (we set here  $\rho = 10^{-6}$ ) in the gap of width  $\lambda = 0.4$ –2 nm can change the diagram shown in Fig. 1(b). The diagrams in Figs. S1–S3, which are calculated for several pressures  $\rho = 1, 10^{-2}, 10^{-4}, 10^{-6}$ , a gap width  $\lambda = 0.2, 0.4$ , and 2 nm, and a film thickness  $h = 50, 25$ , and 10 nm, illustrate the trends shown in Fig. 2 in more detail.

The diagrams in Figs. S1–S3, calculated for the case of zero total field,  $E_{SI} + E_a = 0$ , contain the PE phase, shown by a russet color. The built-in field vanishes at  $\lambda \rightarrow 0$  or/and  $\rho \rightarrow 1$  [see Eq. (10b) for details]. When the value of  $E_{SI}$  increases (either with  $\rho$  deviation from unity or with an in-

crease in  $\lambda$ ), the PE phase continuously transforms in the electret-like FEI phase, the ferroionic features of which are especially pronounced for thin films ( $h < 20$  nm) and wide gaps ( $\lambda > 1$  nm). Since  $E_{SI}$  gradually changes with pressure  $\rho$  and temperature  $T$ , the boundary between the FEI and PE phases is diffuse [e.g., the remainder of PE is shown by a russet color in Fig. 2(c)]. The classification of other FE phases, listed in Table I, remains valid for  $E_{SI} \neq 0$ , with the remark that the FEaa phase includes the component  $P_3$  without hysteresis that is proportional to the acting field  $E_{SI} + E_a$ . Note that the diagrams plotted for  $\rho = 10^{-6}$  coincide with the ones for  $\rho = 10^6$ , which is evident from Eqs. (3) and (9) for the parameters listed in Table III.

The most important differences between the diagram in Fig. 2(a), calculated for a relatively thick film ( $h = 50$  nm) and a narrow gap ( $\lambda = 0.4$  nm), and the diagram in Fig. 1(b) are the strongly curved boundary between the FEr and FEaa phases, the slightly curved boundary between the FEc and FEr phases, and, equally important, the wider region of the FEaa phase in Fig. 1(b). The curved phase boundaries reflect the nonlinear nature of the SH model for the surface charge, and the curvature increases strongly with the decrease in the film thickness [compare Fig. 2(a) for  $h = 50$  nm with Fig. 2(b) for  $h = 25$  nm]. For ultrathin films, the region of FEr phase stability becomes small and acquires the shape of a rounded triangle, and the FEc phase becomes “reentrant,” since the second region of the phase appears at  $250 < T < 350$  K and  $u_m < -0.5\%$  [see Fig. 2(c) for  $h = 10$  nm]. The reentrant



FEC phase appears for wider gaps ( $\lambda = 2$  nm) and borders with FEI and FER phases, at which one of the boundaries is strongly curved [see Fig. 2(d) for  $h = 50$  nm]. The area of the reentrant FEC phase decreases very weakly for thinner films with a wider gap [compare Figs. 2(e) and 2(f) for  $h = 25$  nm and  $h = 10$  nm, respectively].

To summarize, the diagrams shown in Figs. 2(c)–2(f) look very different from the diagram shown in Fig. 1(b), and the most interesting feature is the appearance of FEC reentrant phases and FEI phases. For wide gaps, the reentrant FEC phases have an unusual curved shape, shown in Figs. 2(c)–2(f). The reentrance originates from the surface screening by oxygen ions. Mathematically, the features are defined by the dependence of the coefficient  $b_3$  on the variables  $T$  and  $\rho$  [see Eq. (8a) for details]. The coefficient contains the strongly varying factor  $1 + S(T, \rho, h)$ . The temperature-pressure color maps of the surface charge entropy  $S(T, \rho, h)$  are shown in Figs. 1(c) and 1(d). The behavior of  $S(T, \rho, h)$  defines the nonmonotonic dependence of the coefficient  $b_3$  on  $T$ .  $b_3(T, \rho, h, u_m)$  can change its sign several times for compressive strains  $u_m < 0$  if  $\rho \ll 1$  (or  $\rho \gg 1$ ). In accordance with Table I, the condition  $b_3(T, \rho, h, u_m) = 0$  gives us the boundaries between the PE and FEC phases. However, it appeared that the same condition corresponds to the boundary between the FER and FEaa phases with a very high accuracy [an example of such a boundary is shown by a red line in Fig. 2(f)]. The explanation of the result is the following. Per Table I, the boundary between the FER and FEaa phases is given by the equivalence of their energies,  $-\frac{b_1^2}{(2b_{11}+b_{12})} = \frac{-b_3^2(2b_{11}+b_{12})-4b_1^2b_{33}+4b_1b_3b_{13}}{4(2b_{11}+b_{12})b_{33}-b_{13}^2}$ . Putting  $b_3 = 0$  on the right-hand side, we obtain the expression  $\frac{-b_1^2}{(2b_{11}+b_{12})-\frac{b_{13}^2}{b_{33}}}$ , which is almost equal to the left-hand side, since the strong inequality,  $\frac{b_{13}^2}{b_{33}} \ll 2b_{11} + b_{12}$ , is valid.

Hence the differences between Figs. 2(d)–2(f) and Fig. 1(b) evidently originate from the surface ions, the influence of which is controlled by the parameter  $\rho$  and finite-size effects, whose strength is controlled by the film thicknesses  $h$  and gap width  $\lambda$ , respectively. The reentrant phase and other features are observed for compressed films (e.g., for  $u_m < -0.2\%$ ), since the compressive strain supports the out-of-plane polarization component  $P_3$  [59], and only  $P_3$  is sensitive to the screening provided by the surface ions. Hence, we focus on an analysis of the influence of  $\rho$ ,  $h$ , and  $\lambda$  on the phase diagrams and the polar and dielectric properties of the compressed multiaxial ferroelectric films.

The common features of the diagrams shown in Figs. 2(c)–2(f) are the unusual parabolic-like shape of the reentrant FEC phase region, the straight boundary between the FEI/PE and FEaa phases, the curved boundary between the FEC and FER phases, and a single point, where all stable phases (FEI, FEC, FER, and FEaa) coexist. All these features originate from the surface screening by oxygen ions. Mathematically, the features are defined by the dependences of the coefficients  $b_3$ ,  $b_{33}$ , and  $b_{13}$  on the variables  $T$  and  $\rho$  [see Eqs. (8) for details]. As was discussed above, the coefficients contain the surface charge entropy  $S(T, \rho, h)$ , which diverges at  $T \rightarrow 0$  and decreases monotonically with an increase in  $T$ . As a result, the

coefficient  $b_3$  depends nonmonotonically on  $T$  and can change its value several times at a fixed  $\rho$  value. The condition  $b_3 = 0$  gives us the “reentrant” boundaries between the FEI and FEC phases and the FER and FEaa phases; an example is shown by a red line in Fig. 4(f).

## B. Chemical control of the extrinsic size effect

Typical phase diagrams of a compressed multiaxial FE film in dependence on the temperature  $T$ , relative partial oxygen pressure  $\rho$ , film thickness  $h$ , and gap width  $\lambda$  are shown in Fig. 3. They are calculated for a compressed strain  $u_m = -0.25\%$ . The values of  $T$ ,  $\rho$ ,  $h$ , and  $\lambda$  are listed for each plot. Similar to Fig. 2, the diagrams calculated for the case of a compensated built-in field,  $E_{SI} + E_a = 0$ , contain the PE phase and three FE phases, FEC, FEaa, and FER. When  $E_{SI} \neq 0$ , the PE phase transforms the electret-like FEI phase in thin films. The boundary between the FEI (shown by a sand color) and PE (shown by a russet color) phases is diffuse, especially for a narrow gap ( $\lambda = 0.4$  nm). Different parts of Fig. 3 show how the boundaries of the PE, FEI, and different FE phases depend on the film thickness and gap width.

Figure 3(a) shows the film phase diagram in coordinates  $h$  and  $\rho$ , calculated for room temperature and a narrow gap  $\lambda = 0.4$  nm. Here the PE phase is located at  $\rho$  very close to unity, and the film thickness is less than the critical value,  $h < h_{cr}$ . The FEC phase is stable for  $h > h_{cr}$ , and the critical value  $h_{cr}$  depends strongly on  $\rho$  for thin films, but it becomes  $\rho$ -independent when  $h$  exceeds 35 nm (see the vertical dashed line). The FER phase is stable at  $\rho \ll 1$  and film thickness more than the characteristic value  $h_{FER}$ , which dependence on  $\rho$  is rather weak. The region of FER phase increases very slightly with an increase in  $h$ .

Figure 3(b) is the film phase diagram in coordinates  $\lambda$  and  $\rho$ , calculated for room temperature and a film thickness  $h = 25$  nm. The FEC phase is stable for  $\lambda < \lambda_{cr}$ , and the critical value  $\lambda_{cr}$  is  $\rho$ -independent for narrow gaps, but it becomes  $\rho$ -dependent when  $\lambda$  exceeds 0.6 nm (see the vertical dashed line). The FER phase is stable at  $\rho \ll 1$  and a gap thickness more than the specific value  $\lambda_{FER}$ , which dependence on  $\rho$  is rather weak. The region of FER phase increases very moderately with an increase in  $\lambda$ . Notably, a relatively simple analytical expression for  $\lambda_{cr}$  can be derived from the condition  $b_3 = 0$  [see Eq. (8a)]:

$$\lambda_{cr}(T, \rho, h) \cong \frac{2\varepsilon_0\varepsilon_d h \left( \frac{2Q_{12}u_m}{s_{11}+s_{12}} - a_1(T) \right)}{1 + h \left( a_1(T) - \frac{2Q_{12}u_m}{s_{11}+s_{12}} \right) \sum_{i=1,2} \frac{(eZ_i f_i(T, \rho))^2}{A_i k_B T}}. \quad (13)$$

Figure 3(c) is the film phase diagram in coordinates  $T$  and  $h$ , calculated for  $\rho = 10^{-6}$  and a gap width  $\lambda = 0.4$  nm. The FEaa phase is stable at temperatures  $T < 300$  K and  $h < 22$  nm. The FEaa-FEI boundary is a straight horizontal line, while the FEaa-FER boundary is sharply curved. The FER phase exists at temperatures slightly higher than 300 K and a film thickness higher than 5–20 nm. The FEC phase occupies the widest temperature region (about 200 K in width) between the FER and FE phases. The FEI phase, which becomes almost indistinguishable from the PE phase with an increase in  $h$ ,

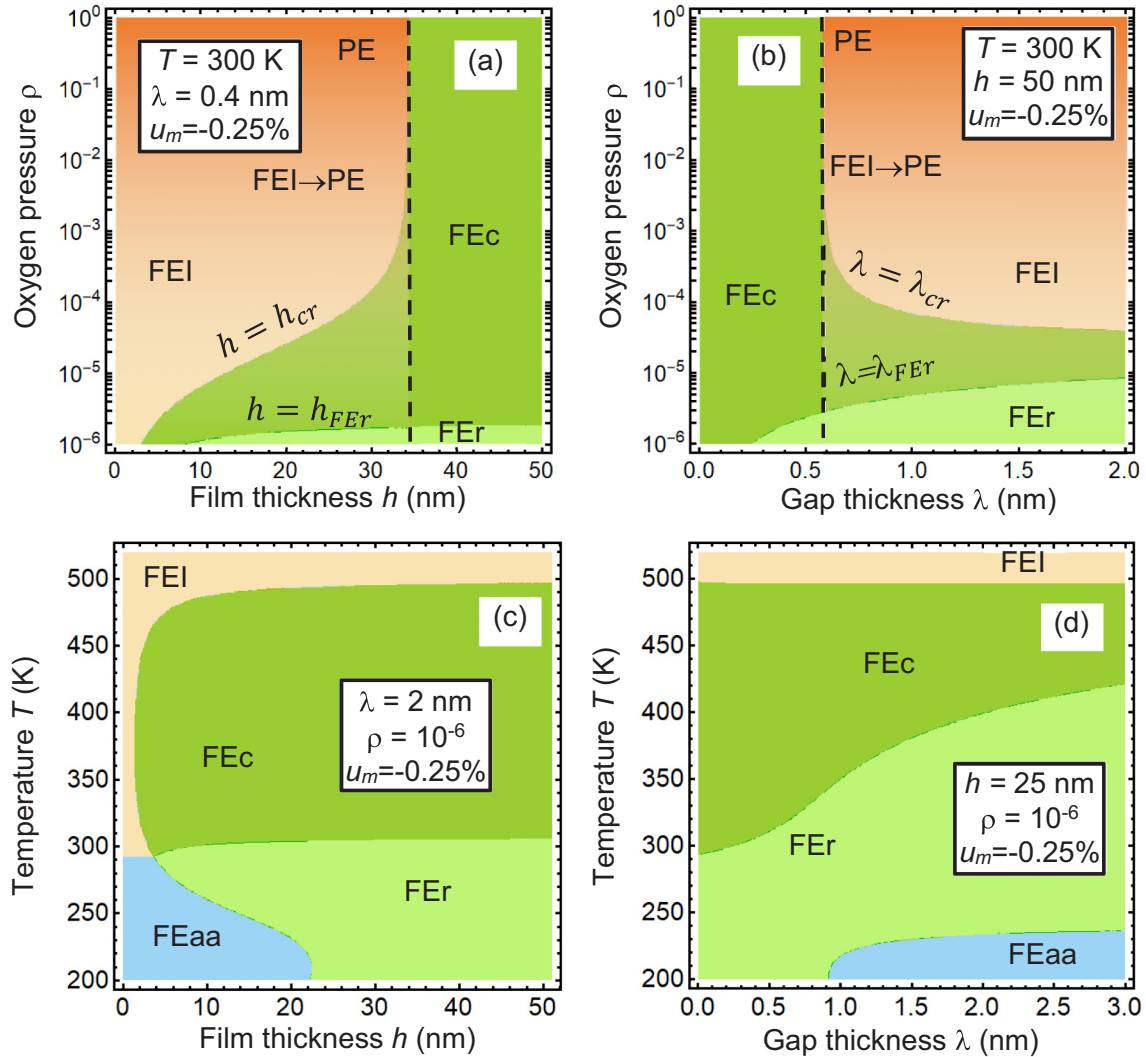


FIG. 3. Typical phase diagrams of a multiaxial FE film in dependence on the temperature  $T$  (a), (b), relative partial oxygen pressure  $\rho$  (c), (d), film thickness  $h$  (a), (c), and gap width  $\lambda$  (b), (d). The values of  $T$ ,  $\rho$ ,  $h$ , and  $\lambda$  are listed for each plot. The mismatch strain  $u_m = -0.25\%$ ,  $U = 0$ ; other parameters are listed in Tables II and III.

occupies the high-temperature region. The four phases (FEI, FEc, FEr, and FEaa) coexist in a single point.

Figure 3(d) is the film phase diagram in coordinates  $T$  and  $\lambda$  calculated for  $\rho = 10^{-6}$  and a film thickness  $h = 25$  nm. The small region of the FEaa phase, which is stable at temperatures  $T < 240$  K and  $\lambda > 0.9$  nm, borders with the FEr phase, which occupies the widest region at the diagram. The FEaa-FEr boundary is a steep curve that saturates with an increase in  $\lambda$ . The FEr phase, which is stable in the temperature range between 300 and 420 K, enlarges its area significantly with a decrease in  $\lambda$ . The FEr-FEc boundary is a smooth curve with a flexion. The FEc phase, which is stable in the temperature range between 300 and 500 K, has a straight boundary with the FEI phase that is a horizontal line  $T = 500$  K. The FEI phase occupies the high-temperature region above 500 K.

Expressions (8a), (9), and (12) explain the  $\lambda$  and  $h$  size effects of the phase diagram shown in Fig. 3. In particular, the interplay between the first term  $\frac{\lambda h}{\epsilon_0(\epsilon_d h + \lambda \epsilon_{33}^b)}$  in the surface

charge entropy  $S(T, \rho, h)$  and the last term  $\frac{\lambda}{\epsilon_0(\epsilon_d h + \lambda \epsilon_{33}^b)}$  in Eq. (8a) is responsible for the monotonic increase followed by the saturation of  $\lambda$ - and  $h$ -dependences of the boundaries between the FEr and FEc phases. Also, the expressions describe the behavior of the FEI-FEc boundary at either  $h < h_{cr}$  or  $\lambda > \lambda_{cr}$  in Figs. 3(a) and 3(b), respectively. These size factors can also explain the shape of the FEI-FEc and FEc-FEr boundaries in Figs. 3(a) and 3(b), respectively. However, the boundaries between the FEaa and FEr phases, which have a complex shape, cannot be described by the above-mentioned size dependences, but rather by a complex dependence of the surface charge entropy  $S(T, \rho, h)$  on the temperature and pressure.

The diagrams in Fig. 3 show the possibility to select actual ranges of the film thickness and the gap width for the observation of different FE and FEI phases, and their unusual sequences, including reentrance, and for the control of the phase diagrams, which is most important for various applications. For the material parameters listed in Tables II

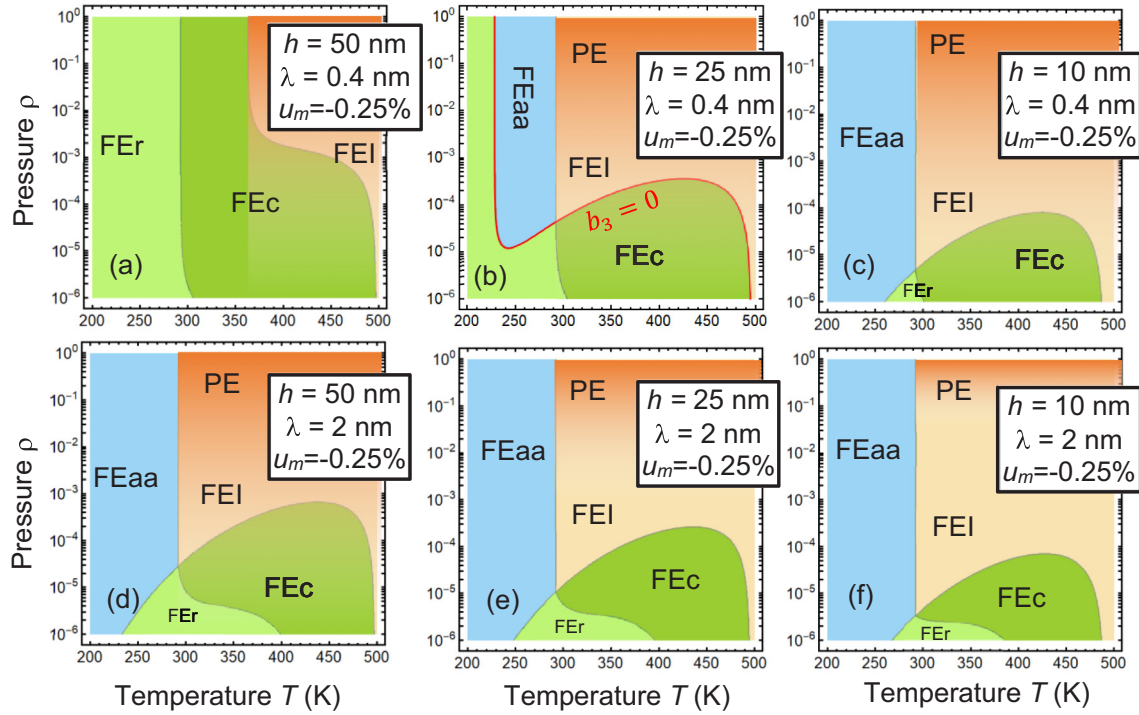


FIG. 4. Typical phase diagrams of a multiaxial FE film in dependence on the temperature  $T$  and relative partial oxygen pressure  $\rho$ . The values of  $h$  and  $\lambda$  are listed for each plot. A red curve in the plot (b) corresponds to the condition  $b_3 = 0$ . The mismatch strain  $u_m = -0.25\%$ ,  $U = 0$ ; other parameters are listed in Tables II and III.

and III, the actual range is  $h = 10\text{--}50$  nm and  $\lambda = 0.4\text{--}2$  nm. In experiment, the film thickness  $h$ , the gap width  $\lambda$ , and the mismatch strain  $u_m$  are fixed, while the temperature  $T$  and relative partial oxygen pressure  $\rho$  are variables. Thus, below we analyze the diagrams in dependence on  $T$  and  $\rho$  for fixed  $h$ ,  $\lambda$ , and  $u_m$  values within the actual range.

Typical phase diagrams of a multiaxial FE film in dependence on the temperature  $T$  and pressure  $\rho$  are shown in Fig. 4 for several film thicknesses  $h$ , and narrow ( $\lambda = 0.4$  nm, the top row) and wider ( $\lambda = 2$  nm, the bottom row) gaps. The diagrams in Figs. S4–S6, which are calculated for several mismatch strains  $u_m$ ,  $\lambda$ , and  $h$ , illustrate the trends shown in Fig. 4 in more detail. For a narrow gap, wide regions of the FEr and FEc phases are stable in thick BaTiO<sub>3</sub> films. The regions of FEI and PE phases are small and located at  $\rho$  close to unity [Fig. 4(a)]. Under the thickness decrease from 50 to 10 nm, the FEr phase gradually transforms into the FEaa phase, and the region of the FEc phase becomes smaller, being substituted by a wider region of the FEI phase [compare Figs. 4(b) and 4(c) with 4(a)].

For a wide gap, the large regions of the FEaa and FEI/PE phases are stable in both thick and thin BaTiO<sub>3</sub> films [see Figs. 4(d)–4(f)]. Under a thickness decrease from 50 to 10 nm, the area of the FEc and FEr phases decreases; in particular, a part of the FEc phase gradually transforms into the FEI phase, and a part of the FEr phase becomes the FEaa phase [compare Figs. 4(d), 4(e), and 4(f)].

The common features of the diagrams shown in Figs. 4(c)–4(f) are the parabolic-like shape of the FEc+FEr phases region, the straight boundary between the FEI/PE and FEaa phases, the curved boundary between FEc and FEr phases,

and a single point, where all stable phases (FEI, FEc, FEr, and FEaa) coexist. As was mentioned above (see the comments regarding Fig. 2), these features originate from the surface screening by oxygen ions. The condition  $b_3 = 0$  gives us the boundaries between FEI and FEc phases, and FEr and FEaa phases; an example is shown by a red line in Fig. 4(b).

### C. Quasistatic field dependences of polarization, dielectric permittivity, and piezoelectric coefficients

To illustrate the polar, dielectric, and piezoelectric properties of the FEI, FEc, FEr, and FEaa phases, which can be stable in thin multiaxial FE films covered with ions, we calculated and analyzed corresponding quasistatic dependences on the applied voltage  $U$  using Eqs. (11). Since we consider that  $\varepsilon_d h \gg \lambda \varepsilon_{33}^b$ , the acting field  $E_a(U, h) = -\frac{\varepsilon_d U}{\varepsilon_d h + \lambda \varepsilon_{33}^b}$  is approximately equal to the external electric field  $E_e = -\frac{U}{h}$  [see Eq. (10c) for details].

Quasistatic dependences of the out-of-plane polarization  $P_3$ , dielectric permittivity  $\varepsilon_{33}$ , and piezoelectric coefficient  $d_{33}$  on the external electric field  $E_e$  are shown in Fig. 5 for several values of the film thickness and partial oxygen pressures. The parameters  $\lambda = 2$  nm,  $u_m = -0.25\%$ , and  $T = 350$  K are chosen in such way that the hysteresis behavior of polarization, the double maxima of permittivity, and the piezoelectric coefficient exist for pressures far from unity,  $\rho = (10^{-6}\text{--}10^{-5})$ , and they disappear for pressures closer to unity,  $\rho = (10^{-4}\text{--}1)$  (compare the different curves in Fig. 5). The dependences with no hysteresis are left-shifted due to the built-in field  $E_{SI}$ , and the shift significantly increases with the decrease in film

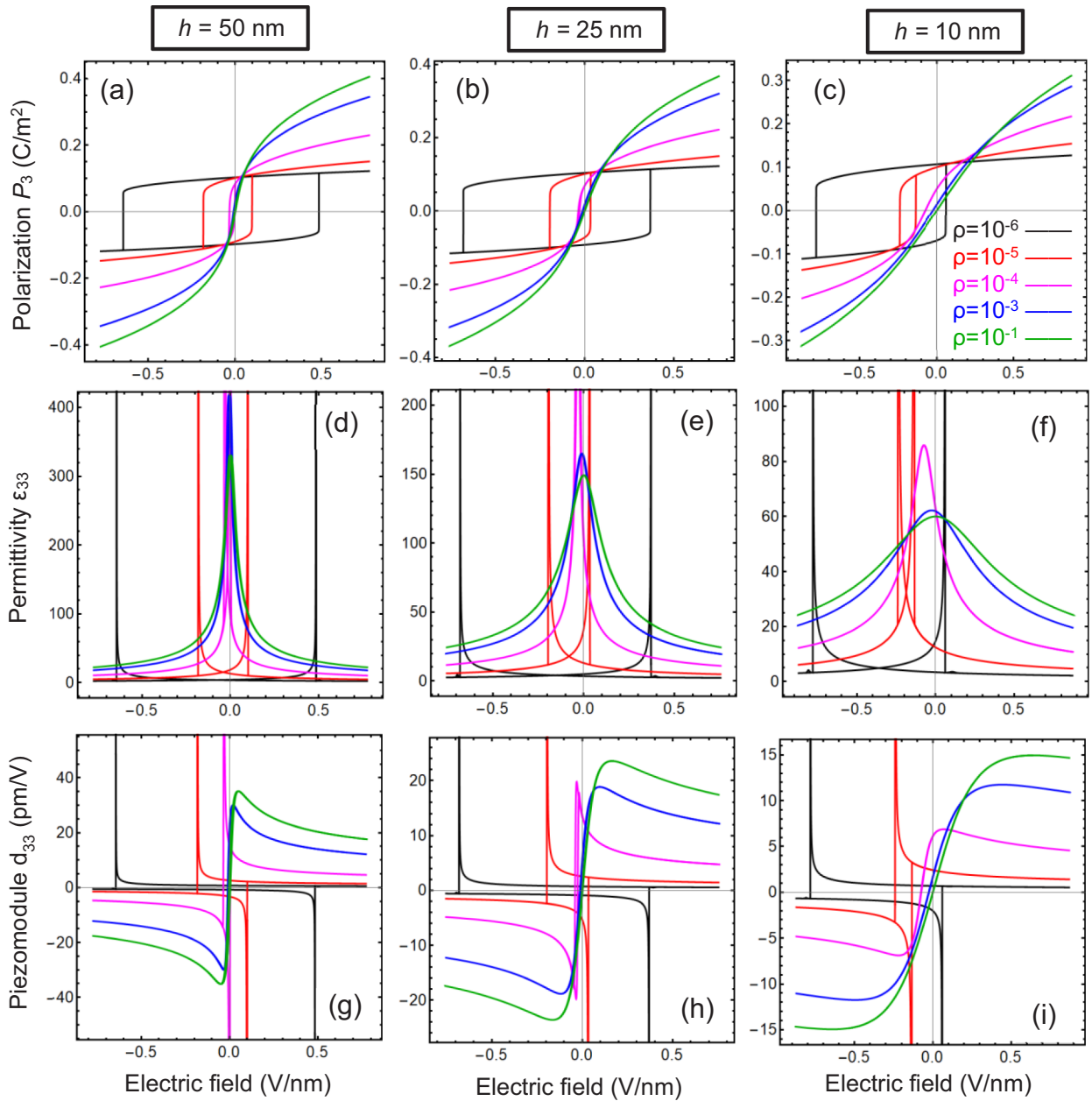


FIG. 5. Quasistatic dependences of the out-of-plane polarization  $P_3$  (a), (b), (c), dielectric permittivity  $\epsilon_{33}$  (d), (e), (f), and piezoelectric coefficient  $d_{33}$  (g), (h), (i) on external electric field  $E_e$  calculated for several values of the film thickness 50 nm (a), (d), (g), 25 nm (b), (e), (h), and 10 nm (c), (f), (i) and partial oxygen pressures  $\rho = 10^{-6}$  (black curves),  $10^{-5}$  (red curves),  $10^{-4}$  (magenta curves),  $10^{-3}$  (blue curves), and  $10^{-1}$  (green curves). Parameters:  $\lambda = 2$  nm,  $u_m = -0.25\%$ , and  $T = 350$  K; other parameters are listed in Tables II and III.

thickness, as explained by the size factor  $\frac{\lambda}{\epsilon_0(\epsilon_d h + \lambda \epsilon_{33}^2)}$  in Eq. (10b) for  $E_{S1}$ . The shift is the most pronounced indicator of the FEI phase. However, the shift exists and becomes noticeable for the FE hysteresis loops calculated at  $\rho \ll 10^{-4}$  when the film becomes thinner (compare the black and red loops in Fig. 5).

It is important for applications that  $d_{33}$  is significantly enhanced for  $\rho = (10^{-6} - 10^{-5})$  in the region of coercive fields [see the red and black curves in Figs. 5(g)–5(i)]. To quantify the enhancement effect, we need to consider (or exclude) the role of domain formation in the presence of surface ions. Indeed, domain formation can appear in multiaxial

FE films [68–71] under incomplete screening of their polarization. In the considered case, domain formation is likely for near-equilibrium oxygen pressures ( $10^{-2} < \rho < 10^2$ ) and wide gaps ( $\lambda > 1$  nm). However, the case  $\rho \rightarrow 1$  is not of our interest, because the reentrant phases and enhanced polar properties correspond to  $\rho = (10^{-6} - 10^{-5})$ .

The field dependences of the in-plane polarization components  $P_1$  and  $P_2$ , dielectric permittivity  $\epsilon_{13}$  and  $\epsilon_{23}$ , and piezoelectric coefficient  $d_{13}$  and  $d_{23}$  are shown in Fig. S8 for the film thickness  $h = 50$ , 25, and 10 nm and relative pressure  $\rho = 10^{-6}$ . The dependences are calculated for the same parameters as the dependences in Fig. 5. The purpose of Fig. S8 is to illustrate the butterflylike shape of  $P_1$  and

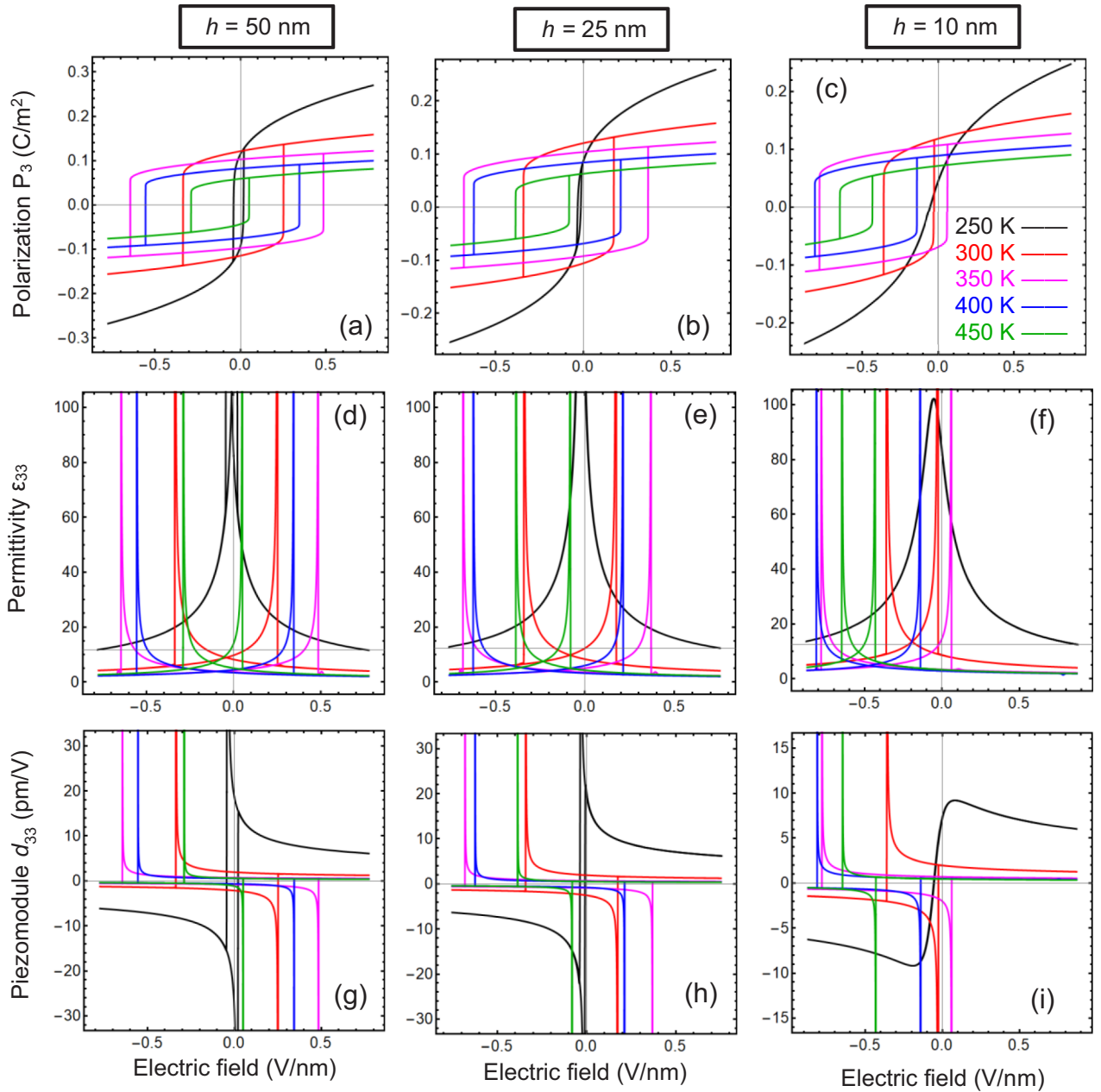


FIG. 6. Quasistatic dependences of the out-of-plane polarization  $P_3$  (a), (b), (c), dielectric constant  $\epsilon_{33}$  (d), (e), (f), and piezoelectric coefficient  $d_{33}$  (g),(h), (i) on external electric field  $E_e$  calculated for several values of film thickness 50 nm (a), (d), (g), 25 nm (b), (e), (h), and 10 nm (c), (f), (i), and temperatures  $T = 250$  (black curves), 300 (red curves), 350 (magenta curves), 400 (blue curves), and 450 K (green curves). Parameters  $\lambda = 2$  nm,  $u_m = -0.25\%$ , and  $\rho = 10^{-6}$ ; other parameters are listed in Tables II and III.

$P_2$  hysteresis loops in the FE<sub>a</sub> and FE<sub>r</sub> phases, the specific hysteresis of  $d_{13}$  and  $d_{23}$  in the phases, and their changes with the decrease in thickness and the variation in oxygen pressure. The butterflylike  $P_{1,2}$  loops, as well as  $d_{13}$  and  $d_{23}$  loops, are also shifted by the built-in field  $E_{S1}$ , and the shift increases with the decrease in film thickness.

Together, the results presented in Figs. 5 and S8 point to the possibility of controlling the appearance and features of ferroelectric, dielectric, and piezoelectric hysteresis in multiaxial FE films covered by surface ions by varying their concentration via the partial oxygen pressure.

Quasistatic dependences of the out-of-plane polarization  $P_3$ , the dielectric constant  $\epsilon_{33}$ , and the piezoelectric coefficient  $d_{33}$  on the external electric field  $E_e$  are shown in Fig. 6 for several values of the film thickness and temperatures,  $\lambda = 2$  nm,  $u_m = -0.25\%$ , and  $\rho = 10^{-6}$ . The parameters are chosen in such way that the hysteresis behavior of polarization, the double maxima of permittivity, and the piezocoefficient exist in the temperature range 290–480 K for thin films and in a slightly wider range 250–500 K for thicker films. The temperature range corresponds mainly to the reentrant FE<sub>c</sub> phase, and so the coercive field is maximal in the middle of the

range (compare the different curves in Fig. 6). Both the curves without hysteresis and the hysteresis loops are left-shifted due to the built-in field  $E_{SI}$ , and the shift increases significantly with the decrease in the film thickness and the increase in temperature. The shift of the curves with no hysteresis is the most pronounced indicator of the FEI phase (compare the black curves for different film thicknesses).

The field dependences of the in-plane polarization components  $P_1$  and  $P_2$ , the dielectric permittivity  $\epsilon_{13}$  and  $\epsilon_{23}$ , and the piezoelectric coefficient  $d_{13}$  and  $d_{23}$  are shown in Figs. S9–S11 for film thickness  $h = 50, 25,$  and  $10$  nm. The dependences are calculated for the same parameters as the dependences in Fig. 6. The purpose of Figs. S9–S11 is to illustrate the transformations of  $P_1$  and  $P_2$   $E$ -dependences, which happen in the FEI, FEaa, and FEr phases with changes of the film thickness and temperature.

Generally, the results presented in Figs. 6 and S9–S11 point to the temperature control of the appearance and features of ferroelectric, dielectric, and piezoelectric hysteresis in multi-axial FE films covered by surface ions.

#### D. Multiobjective Bayesian exploration with Gaussian process

We carried out a detailed investigation of both the phase and the minimum free energy of a multi-axial FE film in dependence on the temperature  $T$  and mismatch strain  $u_m$ , as shown in Fig. 7 with further detailed figures and formulations as explained in Appendix D of the Supplemental Material. The COLAB code is available in [72].

We started by configuring the phase and minimum free-energy map with an exhaustive grid search. Due to the high computational cost, it is feasible only to obtain a low-sampling grid search (here we did a  $10 \times 10$  map). However, it is also evident that in order to understand these functionalities in depth and to identify potentially interesting physics in a given parameter space, a low-sampling grid search is not sufficient. This will only yield a high-level picture, with a likelihood of overlooking some key features (maximum or minimum values) of the functionalities within the unknown parameter space, especially if the key features are confined to a very narrow area. Thus, for the problem of learning different functionalities in an unknown parameter space, a generalized approach is required that has the flexibility to trade off between learning accuracy and cost (computational). These challenges motivated us to develop a multiobjective Bayesian optimization (MOBO) architecture in which first each chosen functionality is replaced with a respective cheap surrogate Gaussian process regression model, and then rapid exploration/exploitation is attempted in order to learn a user-specified interesting domain region through sequential sampling by optimizing a multi-function-based acquisition function, thus reducing the cost of function evaluations. Bayesian optimization (BO) is an emerging field of study in the area of sequential design methods [73–75]. It has been considered to be a global optimization tool with a low computational cost that can be used for design problems that have expensive and/or black-box objective functions. Since BO is a broad approach, and to align to the scope of the paper, we provide the readers with a summarized illustration in the Supplemental Material (Appendix D) for a conceptual understanding. The

BO approach has been widely used in many machine learning problems [76–78]. MOBO is an extension of BO as we considered learning multiple functionalities jointly in MOBO (e.g., phase and energy), instead of a single one in BO.

To date, there are only a few applications of MOBO for material discovery in optimizing multiple target properties, considering both experimental and computer simulated data [79]. MOBO has also been applied for efficient discovery of the targeted materials, performed by a thermodynamically consistent micromechanical model that predicts the materials response based on its composition and microstructure [80]. Recently, a physics-driven MOBO was implemented for the discovery of the optimal Pareto frontier between energy storage and loss in interfacial-controlled ferroelectric materials [50]. Unlike those applications, the goal here is to learn the overall parameter space, thus we are not optimizing the functions but want to learn the overall trend of the functionalities. Thus, we build our acquisition function, suitable for full exploration of both functionalities (phase and free energy) jointly. For all the analysis shown in Fig. 7, the MOBO is started by evaluating 20 randomly selected locations (samples) from the 2–4 LGD model using material parameters of bulk BaTiO<sub>3</sub> and stopped after 230 MOBO-guided evaluations from a dense  $50 \times 50$  map, with a total of 250 expensive evaluations.

Figures 7(a) and 7(b) are the ground-state phase diagram and the free energy, respectively, calculated using a low-sampling ( $10 \times 10$ ) exhaustive grid search for the same parameter space as in Fig. 1(b). As anticipated, the diagram in Fig. 7(a) is a low-resolution analog of Fig. 1(b). We observe four distinct phases: PE, FEc, FEaa, and FEr. Figures 7(c) and 7(d) are GP predicted dense ( $50 \times 50$ ) maps of phase and free energy, respectively. Here the function evaluations were done at the locations represented by filled dots in the figures. Thus, we build the dense map with an evaluation of only 10% of the total number of grids (250 out of 2500). With  $u_m(\%)$  close to zero and with high (low) values of  $T$ , we find the PE (FEr) phase(s). As the absolute value of  $u_m$  increases, the phase changes to FEaa or FEc, respectively. For the respective free-energy map, we obtain a higher-energy value for the PE and FEr phases, and lower energy for the FEaa and FEc phases. Figures S13(a) and S13(b) in the Supplemental Material are the uncertainty maps for the respective GP-predicted maps in Figs. 7(c) and 7(d).

Figures 7(e) and 7(f) are the ground-state phase diagram and the free energy, respectively, calculated using a low-sampling exhaustive grid search for the same parameter space as in Fig. 2(a), and the diagram in Fig. 7(e) is a low-resolution analog of Fig. 2(a). Figures 7(g) and 7(h) are the GP-predicted dense map of phase and free energy, respectively. With  $u_m(\%)$  close to zero and with high (or low) values of  $T$ , we find the PE (or FEr) phase. As the value of  $u_m$  increases in the positive (or negative) direction, we see phase changes to FEaa (or FEc). The trend is similar to the phase map in Fig. 7(d), however the trend in the energy map is very different from Fig. 7(g). Here, we obtain a higher-energy value for the PE, FEaa, and FEr phases and lower energy for the FEc phase. Figures S13(c) and S13(d) in the Supplemental Material are the uncertainty maps for the respective GP predicted maps in Figs. 7(g) and 7(h).

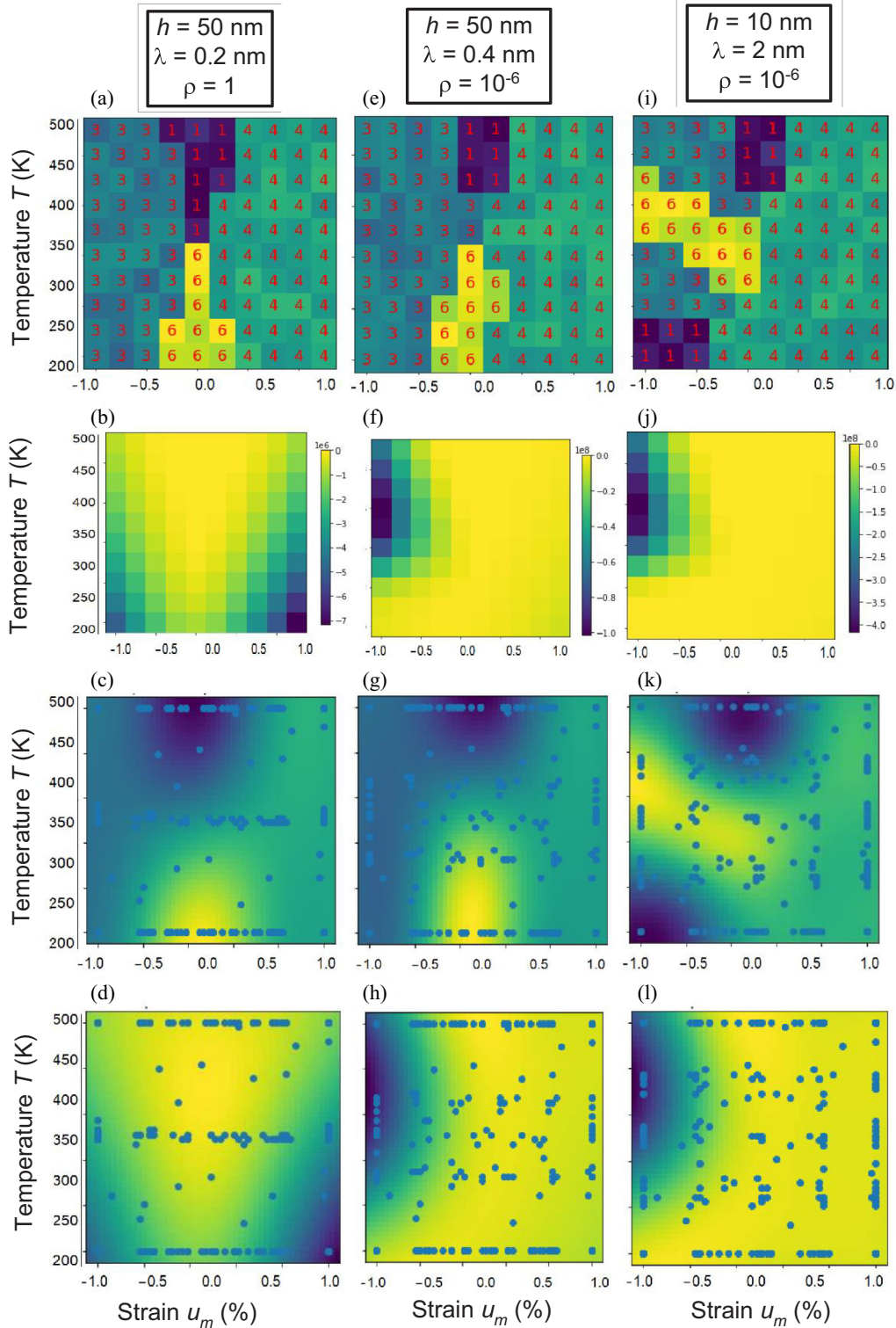


FIG. 7. Joint exploration of the phase and minimum free-energy diagrams of a multiaxial FE film in dependence of the temperature  $T$  and mismatch strain  $u_m$ . Parameter space:  $T$  (K) = [200, 500] and  $u_m$ (%) = [-1, 1]. The values of  $h$ ,  $\lambda$ ,  $\rho$  are the same for each column corresponding to the parameter space for Figs. 1(b), 2(a), and 2(f), respectively. Maps (a), (e), (i) are the ground states of phase diagrams, and maps (b), (f), (j) are the ground states of minimum free-energy diagrams calculated using low-sampling exhaustive grid search; maps (c,g,k) are the predicted phases of dense maps of ground truth maps (a), (e), (i), and the maps (d, h, l) are the predicted energy dense maps of ground truth maps (b), (f), (j). The filled dots in the predicted maps are the locations only where the function evaluation is done to build the respective dense maps of the entire domain space. The numbers printed within the grids of the ground-state phase diagrams are as follows: PE, 1; FEa, 2; FEc, 3; FEaa, 4; FEac, 5; Fer, 6. Actually, FEa and FEac phases are absent. Other parameters are listed in Tables II and III.

Figures 7(i) and 7(j) are the ground-state phase diagram and the free energy, respectively, calculated using a low-sampling exhaustive grid search for the same parameter space as in Fig. 2(f), and the diagram in Fig. 7(i) is a low-resolution analog of Fig. 2(f). Figures 7(k) and 7(l) are the GP-predicted dense map of phase and free energy, respectively. With  $u_m(\%)$  close to zero and with high values of  $T$ , we find the PE phase. We have another region of the PE phase where both values,  $T$  and  $u_m$ , are lower. We find the FEaa phase mostly as  $u_m$  increases in the positive direction and sometimes when  $u_m$  is close to zero. Just like the PE phase, the reentrant FEc phase also has two distinct regions mostly as  $u_m$  increases in the negative direction, where these two FEc regions are separated by the region of the FEr phase. Here, we obtain a higher-energy value for the PE and FEaa phases, and lower energy for the FEc and FEr phases. Figures S13(e) and S13(f) in the Supplemental Material [55] are the uncertainty maps for the respective GP-predicted maps in Figs. 7(k) and 7(l).

To sum up, the LGD-SH description of a multiaxial FE film appears to be very promising for MOBO. Such an approach with its very low computational cost—that allows for high-resolution learning of any unknown space, provides a good balance between accuracy and cost, and has the option to capture the uncertainty in learning the parameter space—builds a key framework for the treatment of potential experiments.

## V. CONCLUSION

Using the LGD-SH approach, we described the electrochemical switching and rotation of a polarization vector in a ferroelectric film covered by surface ions with a charge density related with the partial oxygen pressure. We calculate the phase diagrams, analyze the dependence of polarization components on the applied voltage, and discuss the peculiarities of quasistatic ferroelectric, dielectric, and piezoelectric hysteresis loops in thin strained multiaxial ferroelectric films.

The nonlinear surface screening by oxygen ions makes the phase diagrams very different from the known ones, with the most interesting feature being the appearance of ferroelectric reentrant phases. The common features of the diagrams are the unusual parabolic-like shape of the reentrant FEc phase region, the straight boundary between the FEI/PE and FEaa phases, the curved boundary between the FEc and FEr phases, and a single point, where all stable phases (FEI, FEc, FEr, and FEaa) coexist. The LGD-SH description of a multiaxial FE film appears very promising for MOBO, being important for the treatment of potential experiments.

Both hysteresis-less curves and hysteresis loops of polarization vector and piezoelectric tensor components are shifted due to the built-in field induced by the surface ions, and the

shift significantly increases with the film thickness decrease and temperature increase. The shift of the hysteresis-less curves is the most pronounced indicator of the FEI phase. Obtained results point to the possibility of controlling the appearance and features of ferroelectric, dielectric, and piezoelectric hysteresis in multiaxial FE films covered by surface ions by varying their concentration via the partial oxygen pressure.

We also predict the enhanced properties at the polarization rotation, and to quantify the effect, we need to explore the role of domain formation in the presence of surface defects, which can appear in multiaxial FE films [68–70] under incomplete screening conditions. In the considered case, domain formation is likely for the near-equilibrium relative oxygen pressures and wide gaps. However, the region of pressures is far from our interest, because the reentrant phases and enhanced polar properties correspond to high oxygen excess or deficiency. Not less important can be the interplay between the proximity to the polarization rotation boundary and the emergence of nanoscale phase separation [81].

## ACKNOWLEDGMENTS

The authors are deeply indebted to the referees for their great efforts to help us to improve the work, including results correction and explanation. This effort is based upon work supported by the U.S. Department of Energy, Office of Science, Office of Basic Energy Sciences Energy Frontier Research Centers program under Award No. DE-SC0021118 (S.V.K. and A.B.), and it was performed at the Oak Ridge National Laboratory's Center for Nanophase Materials Sciences (CNMS), a U.S. Department of Energy, Office of Science User Facility. The work of A.N.M. and N.V.M. is supported by the National Academy of Sciences of Ukraine (Grant Application No. 1230). This manuscript has been authored by UT-Battelle, LLC, under Contract No. DE-AC0500OR22725 with the U.S. Department of Energy. The U.S. Government retains and the publisher, by accepting the article for publication, acknowledges that the U.S. Government retains a nonexclusive, paid up, irrevocable, worldwide license to publish or reproduce the published form of this manuscript, or allow others to do so, for the U.S. Government purposes. The Department of Energy will provide public access to these results of federally sponsored research in accordance with the DOE Public Access Plan [82].

S.V.K. and A.N.M. generated the research idea. A.N.M. proposed the theoretical model, derived analytical results, and interpreted numerical results, obtained by E.A.E and H.V.S. A.B. performed MOBO analysis. A.N.M. and S.V.K. wrote the manuscript draft. All coauthors worked on a discussion of the results and improving the manuscript.

- 
- [1] S. Mathews, R. Ramesh, T. Venkatesan, and J. Benedetto, Ferroelectric field effect transistor based on epitaxial perovskite heterostructures, *Science* **276**, 238 (1997).  
 [2] S. L. Miller and P. J. McWhorter, Physics of the ferroelectric nonvolatile memory field effect transistor, *J. Appl. Phys.* **72**, 5999 (1992).

- [3] C. A. P. Dearaujo, J. D. Cuchiaro, L. D. McMillan, M. C. Scott, and J. F. Scott, Fatigue-free ferroelectric capacitors with platinum electrodes, *Nature (London)* **374**, 627 (1995).  
 [4] J. F. Scott and C. A. P. Dearaujo, Ferroelectric memories, *Science* **246**, 1400 (1989).



- [5] O. Auciello, J. F. Scott, and R. Ramesh, The physics of ferroelectric memories, *Phys. Today* **51**(7), 22 (1998).
- [6] O. Kolosov, A. Gruverman, J. Hatano, K. Takahashi, and H. Tokumoto, Nanoscale Visualization and Control of Ferroelectric Domains by Atomic Force Microscopy, *Phys. Rev. Lett.* **74**, 4309 (1995).
- [7] K. Franke and M. Wehnacht, Evaluation of electrically polar substances by electric scanning force microscopy. Part I: Measurement signals due to Maxwell stress, *Ferroelectron. Lett. Sect.* **19**, 25 (1995).
- [8] L. M. Eng, M. Friedrich, J. Fousek, and P. Gunter, Scanning force microscopy of ferroelectric crystals, *Ferroelectrics* **186**, 49 (1996).
- [9] C. H. Ahn, T. Tybell, L. Antognazza, K. Char, R. H. Hammond, M. R. Beasley, O. Fischer, and J. M. Triscone, Local, nonvolatile electronic writing of epitaxial  $\text{Pb}(\text{Zr}_{0.52}\text{Ti}_{0.48})\text{O}_3/\text{SrRuO}_3$  heterostructures, *Science* **276**, 1100 (1997).
- [10] E. Y. Tsymbal and H. Kohlstedt, Tunneling across a ferroelectric, *Science* **313**, 181 (2006).
- [11] P. Maksymovych, S. Jesse, P. Yu, R. Ramesh, A. P. Baddorf, and S. V. Kalinin, Polarization control of electron tunneling into ferroelectric surfaces, *Science* **324**, 1421 (2009).
- [12] M. Bibes, J. E. Villegas, and A. Barthelemy, Ultrathin oxide films and interfaces for electronics and spintronics, *Adv. Phys.* **60**, 5 (2011).
- [13] T. S. Boscke, S. Teichert, D. Brauhaus, J. Muller, U. Schroder, U. Bottger, and T. Mikolajick, Phase transitions in ferroelectric silicon doped hafnium oxide, *Appl. Phys. Lett.* **99**, 112904 (2011).
- [14] J. Muller, T. S. Boscke, D. Brauhaus, U. Schroder, U. Bottger, J. Sundqvist, P. Kucher, T. Mikolajick, and L. Frey, Ferroelectric  $\text{Zr}_{0.5}\text{Hf}_{0.5}\text{O}_2$  thin films for nonvolatile memory applications, *Appl. Phys. Lett.* **99**, 112901 (2011).
- [15] M. H. Park, C. C. Chung, T. Schenk, C. Richter, M. Hoffmann, S. Wirth, J. L. Jones, T. Mikolajick, and U. Schroeder, Origin of temperature-dependent ferroelectricity in Si-doped  $\text{HfO}_2$ , *Adv. Electron. Mater.* **4**, 1700489 (2018).
- [16] K. Ferri, S. Bachu, W. Zhu, M. Imperatore, J. Hayden, N. Alem, N. Giebink, S. Trolrier-McKinstry, and J.-P. Maria, Ferroelectrics everywhere: Ferroelectricity in magnesium substituted zinc oxide thin films, *J. Appl. Phys.* **130**, 044101 (2021).
- [17] W. Zhu, J. Hayden, F. He, J.-I. Yang, P. Tipsawat, M. D. Hossain, J.-P. Maria, and S. Trolrier-McKinstry, Strongly temperature dependent ferroelectric switching in  $\text{AlN}$ ,  $\text{Al1-XScxN}$ , and  $\text{Al1-XBxN}$  thin films, *Appl. Phys. Lett.* **119**, 062901 (2021).
- [18] Y. Song *et al.*, Thermal conductivity of aluminum scandium nitride for 5G mobile applications and beyond, *ACS Appl. Mater. Interfaces* **13**, 19031 (2021).
- [19] E. V. Chensky and V. V. Tarasenko, Theory of phase transitions to inhomogeneous states in finite ferroelectrics in an external electric field, *Sov. Phys. JETP* **56**, 618 (1982) [*Zh. Eksp. Teor. Fiz.* **83**, 1089 (1982)].
- [20] A. K. Tagantsev, L. E. Cross, and J. Fousek, *Domains in Ferroic Crystals and Thin Films* (Springer, New York, 2010).
- [21] S. V. Kalinin and D. A. Bonnell, Screening phenomena on oxide surfaces and its implications for local electrostatic and transport measurements, *Nano Lett.* **4**, 555 (2004).
- [22] A. K. Tagantsev and G. Gerra, Interface-induced phenomena in polarization response of ferroelectric thin films, *J. Appl. Phys.* **100**, 051607 (2006).
- [23] S. V. Kalinin, Y. Kim, D. D. Fong, and A. N. Morozovska, Surface screening mechanisms in ferroelectric thin films and its effect on polarization dynamics and domain structures, *Rep. Prog. Phys.* **81**, 036502 (2018).
- [24] M. Stengel and N. A. Spaldin, Origin of the dielectric dead layer in nanoscale capacitors, *Nature (London)* **443**, 679 (2006).
- [25] N. Domingo, I. Gaponenko, K. Cordero-Edwards, N. Stucki, V. Pérez-Dieste, C. Escudero, E. Pach, A. Verdaguer, and P. Paruch, Surface charged species and electrochemistry of ferroelectric thin films, *Nanoscale* **11**, 17920 (2019).
- [26] J. E. Spanier, A. M. Kolpak, J. J. Urban, I. Grinberg, L. Ouyang, W. S. Yun, A. M. Rappe, and H. Park, Ferroelectric phase transition in individual single-crystalline  $\text{BaTiO}_3$  nanowires, *Nano Lett.* **6**, 735 (2006).
- [27] H. T. Yi, T. Choi, S. G. Choi, Y. S. Oh, and S. W. Cheong, Mechanism of the switchable photovoltaic effect in ferroelectric  $\text{BiFeO}_3$ , *Adv. Mater.* **23**, 3403 (2011).
- [28] A. L. Kholkin, S. O. Iakovlev, and J. L. Baptista, Direct effect of illumination on ferroelectric properties of lead zirconate titanate thin films, *Appl. Phys. Lett.* **79**, 2055 (2001).
- [29] R. Shao, M. P. Nikiforov, and D. A. Bonnell, Photoinduced charge dynamics on  $\text{BaTiO}_3$  (001) surface characterized by scanning probe microscopy, *Appl. Phys. Lett.* **89**, 112904 (2006).
- [30] S. V. Kalinin, D. A. Bonnell, T. Alvarez, X. Lei, Z. Hu, R. Shao, and J. H. Ferris, Ferroelectric lithography of multicomponent nanostructures, *Adv. Mater.* **16**, 795 (2004).
- [31] S. V. Kalinin, D. A. Bonnell, T. Alvarez, X. Lei, Z. Hu, J. H. Ferris, Q. Zhang, and S. Dunn, Atomic polarization and local reactivity on ferroelectric surfaces: A new route toward complex nanostructures, *Nano Lett.* **2**, 589 (2002).
- [32] L. Wang, S. Liu, X. Feng, C. Zhang, L. Zhu, J. Zhai, Y. Qin, and Z. L. Wang, Flexoelectronics of centrosymmetric semiconductors, *Nat. Nanotechnol.* **15**, 661 (2020).
- [33] L. Shu, S. Ke, L. Fei, W. Huang, Z. Wang, J. Gong, X. Jiang, L. Wang, F. Li, S. Lei, and Z. Rao, Photoflexoelectric effect in halide perovskites, *Nat. Mater.* **19**, 605 (2020).
- [34] D. Kim, L. Collins, R. K. Vasudevan, S. Neymeyer, M. H. Ann, J. H. Kim, A. Morozovska, E. A. Eliseev, M. Ziatdinov, S. V. Kalinin, and M. Ahmadi, Exploring responses of contact-Kelvin probe force microscopy in triple cation double halide perovskites, *J. Phys. Chem. C* **125**, 12355 (2021).
- [35] E. A. Eliseev, A. N. Morozovska, G. S. Svechnikov, E. L. Rumyantsev, E. I. Shishkin, V. Y. Shur, and S. V. Kalinin, Screening and retardation effects on  $180^\circ$ -domain wall motion in ferroelectrics: Wall velocity and nonlinear dynamics due to polarization-screening charge interaction, *Phys. Rev. B* **78**, 245409 (2008).
- [36] A. N. Morozovska, E. A. Eliseev, I. S. Vorotiahin, M. V. Silibin, S. V. Kalinin, and N. V. Morozovsky, Control of polarization hysteresis temperature behavior by surface screening in thin ferroelectric films, *Acta Mater.* **160**, 57 (2018).
- [37] J. D. Baniecki, J. S. Cross, M. Tsukada, and J. Watanabe,  $\text{H}_2\text{O}$  vapor-induced leakage degradation of  $\text{Pb}(\text{Zr},\text{Ti})\text{O}_3$  thin-film capacitors with Pt and  $\text{IrO}_2$  electrodes, *Appl. Phys. Lett.* **81**, 3837 (2002).

- [38] Y. Gu, K. Xu, C. Song, X. Zhong, H. Zhang, H. Mao, M. S. Saleem, J. Sun, W. Liu, Z. Zhang, F. Pan, and J. Zhu, Oxygen-valve formed in cobaltite-based heterostructures by ionic liquid and ferroelectric dual-gating, *ACS Appl. Mater. Interfaces* **11**, 19584 (2019).
- [39] N. C. Bristowe, M. Stengel, P. B. Littlewood, J. M. Pruneda, and E. Artacho, Electrochemical ferroelectric switching: Origin of polarization reversal in ultrathin films, *Phys. Rev. B* **85**, 024106 (2012).
- [40] R. V. Wang, D. D. Fong, F. Jiang, M. J. Highland, P. H. Fuoss, C. Thompson, A. M. Kolpak, J. A. Eastman, S. K. Streiffer, A. M. Rappe, and G. B. Stephenson, Reversible Chemical Switching of a Ferroelectric Film, *Phys. Rev. Lett.* **102**, 047601 (2009).
- [41] D. D. Fong, A. M. Kolpak, J. A. Eastman, S. K. Streiffer, P. H. Fuoss, G. B. Stephenson, C. Thompson, D. M. Kim, K. J. Choi, C. B. Eom, I. Grinberg, and A. M. Rappe, Stabilization of Monodomain Polarization in Ultrathin PbTiO<sub>3</sub> Films, *Phys. Rev. Lett.* **96**, 127601 (2006).
- [42] M. J. Highland, T. T. Fister, M.-I. Richard, D. D. Fong, P. H. Fuoss, C. Thompson, J. A. Eastman, S. K. Streiffer, and G. B. Stephenson, Polarization Switching Without Domain Formation at the Intrinsic Coercive Field in Ultrathin Ferroelectric PbTiO<sub>3</sub>, *Phys. Rev. Lett.* **105**, 167601 (2010).
- [43] M. J. Highland, T. T. Fister, D. D. Fong, P. H. Fuoss, C. Thompson, J. A. Eastman, S. K. Streiffer, and G. B. Stephenson, Equilibrium Polarization of Ultrathin PbTiO<sub>3</sub> with Surface Compensation Controlled by Oxygen Partial Pressure, *Phys. Rev. Lett.* **107**, 187602 (2011).
- [44] G. B. Stephenson and M. J. Highland, Equilibrium and stability of polarization in ultrathin ferroelectric films with ionic surface compensation, *Phys. Rev. B* **84**, 064107 (2011).
- [45] S. M. Yang, A. N. Morozovska, R. Kumar, E. A. Eliseev, Y. Cao, L. Mazet, N. Balke, S. Jesse, R. Vasudevan, C. Dubourdieu, and S. V. Kalinin, Mixed electrochemical-ferroelectric states in nanoscale ferroelectrics, *Nat. Phys.* **13**, 812 (2017).
- [46] A. N. Morozovska, E. A. Eliseev, N. V. Morozovsky, and S. V. Kalinin, Ferroionic states in ferroelectric thin films, *Phys. Rev. B* **95**, 195413 (2017).
- [47] A. N. Morozovska, E. A. Eliseev, N. V. Morozovsky, and S. V. Kalinin, Piezoresponse of ferroelectric films in ferroionic states: Time and voltage dynamics, *Appl. Phys. Lett.* **110**, 182907 (2017).
- [48] A. N. Morozovska, E. A. Eliseev, A. I. Kurchak, N. V. Morozovsky, R. K. Vasudevan, M. V. Strikha, and S. V. Kalinin, Effect of surface ionic screening on polarization reversal scenario in ferroelectric thin films: Crossover from ferroionic to antiferroionic states, *Phys. Rev. B* **96**, 245405 (2017).
- [49] A. N. Morozovska, E. A. Eliseev, A. Biswas, N. V. Morozovsky, and S. V. Kalinin, Effect of Surface Ionic Screening on Polarization Reversal and Phase Diagrams in Thin Antiferroelectric Films for Information and Energy Storage, *Phys. Rev. Appl.* **16**, 044053 (2021).
- [50] A. Biswas, A. N. Morozovska, M. Ziatdinov, E. A. Eliseev, and S. V. Kalinin, Multi-objective Bayesian optimization of ferroelectric materials with interfacial control for memory and energy storage applications, *J. Appl. Phys.* **130**, 204102 (2021).
- [51] P. Aguado-Puente, P. Garcia-Fernandez, and J. Junquera, Interplay of Couplings between Antiferrodistortive, Ferroelectric, and Strain Degrees of Freedom in Monodomain PbTiO<sub>3</sub>/SrTiO<sub>3</sub> Superlattices, *Phys. Rev. Lett.* **107**, 217601 (2011).
- [52] J. L. Jones, E. B. Slamovich, and K. J. Bowman, Domain texture distributions in tetragonal lead zirconate titanate by x-ray and neutron diffraction, *J. Appl. Phys.* **97**, 034113 (2005).
- [53] V. Westphal, W. Kleemann, and M. D. Glinchuk, Diffuse Phase Transitions and Random-Field-Induced Domain States of the “relaxor” Ferroelectric PbMg<sub>1/3</sub>Nb<sub>2/3</sub>O<sub>3</sub>, *Phys. Rev. Lett.* **68**, 847 (1992).
- [54] M. D. Glinchuk and V. A. Stephanovich, Dynamic properties of relaxor ferroelectrics, *J. Appl. Phys.* **85**, 1722 (1999).
- [55] See Supplemental Material at <http://link.aps.org/supplemental/10.1103/PhysRevB.105.094112> for mathematical details and additional phase diagrams.
- [56] D. G. Schlom, L.-Q. Chen, C.-B. Eom, K. M. Rabe, S. K. Streiffer, and J.-M. Triscone, Strain tuning of ferroelectric thin films, *Ann. Rev. Mater. Res.* **37**, 589 (2007).
- [57] A. K. Tagantsev, Landau expansion for ferroelectrics: Which variable to use? *Ferroelectrics* **375**, 19 (2008).
- [58] C. H. Woo and Y. Zheng, Depolarization in modeling nanoscale ferroelectrics using the Landau free energy functional, *Appl. Phys. A* **91**, 59 (2008).
- [59] N. A. Pertsev, A. G. Zembilgotov, and A. K. Tagantsev, Effect of Mechanical Boundary Conditions on Phase Diagrams of Epitaxial Ferroelectric Thin Films, *Phys. Rev. Lett.* **80**, 1988 (1998).
- [60] M. Marvan and J. Fousek, Electrostatic energy of ferroelectrics with nonhomogeneous distributions of polarization and free charges, *Phys. Status Solidi B* **208**, 523 (1998).
- [61] K. Y. Foo and B. H. Hameed, Insights into the modeling of adsorption isotherm systems, *Chem. Eng. J.* **156**, 2 (2010).
- [62] A. I. Kurchak, A. N. Morozovska, E. A. Eliseev, S. V. Kalinin, and M. V. Strikha, Nontrivial temperature behavior of the carriers concentration in the nano-structure graphene channel - ferroelectric substrate with domain walls, *Acta Mater.* **155**, 302 (2018).
- [63] Y. Cao and S. V. Kalinin, Phase-field modeling of chemical control of polarization stability and switching dynamics in ferroelectric thin films, *Phys. Rev. B* **94**, 235444 (2016).
- [64] J. Hlinka and P. Márton, Phenomenological model of 90-degree domain wall in BaTiO<sub>3</sub> type ferroelectrics, *Phys. Rev. B* **74**, 104104 (2006).
- [65] A. J. Bell, Phenomenologically derived electric field-temperature phase diagrams and piezoelectric coefficients for single crystal barium titanate under fields along different axes, *J. Appl. Phys.* **89**, 3907 (2001).
- [66] D. Berlincourt and H. Jaffe, Elastic and piezoelectric coefficients of single-crystal barium titanate, *Phys. Rev.* **111**, 143 (1958).
- [67] <https://www.wolfram.com/mathematica>; <https://notebookarchive.org/2021-09-54b5fk4>.
- [68] S. K. Streiffer, J. A. Eastman, D. D. Fong, C. Thompson, A. Munkholm, M. V. Ramana Murty, O. Auciello, G. R. Bai, and G. B. Stephenson, Observation of Nanoscale 180° Stripe Domains in Ferroelectric PbTiO<sub>3</sub> Thin Films, *Phys. Rev. Lett.* **89**, 067601 (2002).
- [69] J. S. Speck and W. Pompe, Domain configurations due to multiple misfit relaxation mechanisms in epitaxial ferroelectric thin films. I. Theory, *J. Appl. Phys.* **76**, 466 (1994).

- [70] J. S. Speck, A. Seifert, W. Pompe, and R. Ramesh, Domain configurations due to multiple misfit relaxation mechanisms in epitaxial ferroelectric thin films. II. Experimental verification and implications, *J. Appl. Phys.* **76**, 477 (1994).
- [71] J. S. Speck, A. C. Daykin, A. Seifert, A. E. Romanov, and W. Pompe, Domain configurations due to multiple misfit relaxation mechanisms in epitaxial ferroelectric thin films. III. Interfacial defects and domain misorientations, *J. Appl. Phys.* **78**, 1696 (1995).
- [72] [https://github.com/arpanbiswas52/PaperNotebooks/blob/main/BTO\\_GPexplore.ipynb](https://github.com/arpanbiswas52/PaperNotebooks/blob/main/BTO_GPexplore.ipynb).
- [73] D. R. Jones, A taxonomy of global optimization methods based on response surfaces, *J. Glob. Optim.* **21**, 345 (2001).
- [74] K. Yang, M. Emmerich, A. Deutz, and T. Bäck, Multi-objective Bayesian global optimization using expected hypervolume improvement gradient, *Swarm Evol. Comput.* **44**, 945 (2019).
- [75] A. Biswas, C. Fuentes, and C. Hoyle, A multi-objective Bayesian optimization approach using the weighted Tchebycheff method, *ASME. J. Mech. Des.* **144**, 011703 (2022).
- [76] D. Lizotte, T. Wang, M. Bowling, and D. Schuurmans, Automatic gait optimization with Gaussian process regression, *IJCAI* **7**, 944 (2007).
- [77] V. M. Cora, *Model-based Active Learning in Hierarchical Policies* (University of British Columbia, 2008).
- [78] M. Frean and P. Boyle, Using Gaussian processes to optimize expensive functions, in *AI 2008: Advances in Artificial Intelligence*, edited by W. Wobcke and M. Zhang, Lecture Notes in Computer Science (Springer, Berlin, 2008), pp. 258–267.
- [79] A. M. Gopakumar, P. V. Balachandran, D. Xue, J. E. Gubernatis, and T. Lookman, Multi-objective optimization for materials discovery via adaptive design, *Sci. Rep.* **8**, 3738 (2018).
- [80] A. Solomou, G. Zhao, S. Boluki, J. K. Joy, X. Qian, I. Karaman, R. Arróyave, and D. C. Lagoudas, Multi-objective Bayesian materials discovery: Application on the discovery of precipitation strengthened NiTi shape memory alloys through micromechanical modeling, *Mater. Design* **160**, 810 (2018).
- [81] Y.-D. Liou *et al.*, Deterministic optical control of room temperature multiferroicity in BiFeO<sub>3</sub> thin films, *Nat. Mater.* **18**, 580 (2019).
- [82] <http://energy.gov/downloads/doe-public-access-plan>.